Deep Weakly-Supervised Learning Methods for Classification and Localization in Histology Images: A Survey

Jérôme Rony[1], **Soufiane Belharbi**[1], **Jose Dolz**[2], **Ismail Ben Ayed**[1], **Luke McCaffrey**[3], **Eric Granger**[1]

[1] LIVIA, Department of Systems Engineering, École de technologie supérieure (Université du Québec), Montreal, Canada

[2] LIVIA, Department of Software and IT Engineering, École de technologie supérieure (Université du Québec), Montreal, Canada

[3] Rosalind and Morris Goodman Cancer Research Centre, Dept. of Oncology, McGill University, Montreal, Canada

Email: jerome.rony.1@etsmtl.net, soufiane.belharbi.1@ens.etsmtl.ca, jose.dolz@etsmtl.ca, ismail.benayed@etsmtl.ca, luke.mccaffrey@mcgill.ca, eric.granger@etsmtl.ca

ABSTRACT

Using state-of-the-art deep learning models for cancer diagnosis presents several challenges related to the nature and availability of labeled histology images. In particular, cancer grading and localization in these images normally relies on both image- and pixel-level labels, the latter requiring a costly annotation process. In this survey, deep weakly-supervised learning (WSL) models are investigated to identify and locate diseases in histology images, without the need for pixel-level annotations. Given training data with image-level labels, these models allow to simultaneously classify histology images and yield pixel-wise localization scores, thereby identifying the corresponding regions of interest. These models are organized into two main approaches that differ in their mechanism for building attention maps to localize salient regions – (1) bottom-up approaches based on forward-pass information through a network, either by spatial pooling of representations/scores, or by detecting class regions; and (2) top-down approaches based on backward-pass information within a network, inspired by human visual attention. Since relevant WSL models have mainly been investigated within the computer vision community, and validated on natural scene images, we assess the extent to which they apply to histology images which have challenging properties, e.g. very large size, non-salient and highly unstructured regions, stain heterogeneity, and coarse/ambiguous labels. The most relevant models for deep WSL (e.g. Class Activation Maps and Deep Multi Instance Learning models) are compared experimentally in terms of accuracy (classification and pixel-wise localization) on several public benchmark histology datasets for breast and colon cancer (BACH ICIAR 2018, BreakHis, CAMELYON16, and GlaS). Furthermore, for large-scale evaluation of WSL models on histology images, we propose a protocol to construct WSL datasets from Whole Slide Imaging, with publicly available deterministic code and coordinates of the sampled patches. Results indicate that several deep learning models can provide a high level of classification accuracy, although accurate pixel-wise localization of cancer regions remains an issue for such images.

Keywords: Medical/Histology Image Analysis, Computer-Aided Diagnosis, Deep Learning, Weakly Supervised Learning, Image Classification, Pixel-Wise Localization, Multiple Instance Learning

1 Introduction

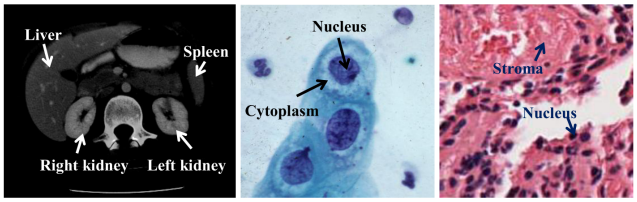

Figure 1: Examples of a radiology computed tomography (CT) image (left), which operates at whole body and tissue, a cytology images (middle), which operates at cellular level, and a histology image (right), which operates at tissue and cell level. (Credit: He et al. (2010; 2012)).

The advent of Whole Slide Imaging (WSI) scanners (He et al., 2012) has opened new possibilities in pathology image analysis (He et al., 2012; Madabhushi, 2009). Histology slides provide more comprehensive views of diseases and their effect on tissue (Hipp et al., 2011) since their preparation preserves the underlying tissue structure (He et al., 2012) (see Fig. 1). For instance, some disease characteristics (e.g. lymphatic infiltration of cancer) may be predicted using only histology images (Gurcan et al., 2009). The analysis of a histology image remains the gold standard in diagnosing several diseases including most types of cancer (He et al., 2012; Gurcan et al., 2009; Veta et al., 2014). Breast cancer is the most prevalent cancer in women worldwide, and medical imaging systems are a primary diagnosis tool for its early detection (Daisuke and Shumpei, 2018; Veta et al., 2014; Xie et al., 2019).

Cancer is mainly diagnosed by pathologists who analyze WSIs to identify and assess epithelial cells organized into ducts, lobules, or malignant clusters, and embedded within a heterogeneous stroma. Manual analysis of histology tissues depends heavily on the expertise and experience of histopathologists. Such manual interpretation is time consuming and difficult to grade in a reproducible manner. Analyzing WSIs from digitized histology slides enables facilitated, and potentially automated, Computer-Aided Diagnosis (CAD) in pathology, where the main goal is to confirm the presence or absence of disease and to grade or measure disease progression.

Given the large numbers of digitized exams, automated systems have become a part of the routine clinical detection of breast cancer (Tang et al., 2009). Automated analysis of the spatial structures in histology images could be traced back to the early works in (Bartels et al., 1992; Hamilton et al., 1994; Weind et al., 1998). Different techniques for image processing and machine learning (ML) have been investigated for identifying discriminative structures and classifying histology images (He et al., 2012), including thresholding (Gurcan et al., 2006; Petushi et al., 2006), active contours (Bamford and Lovell, 2001), Bayesian classifiers (Naik et al., 2007), graphs to model spatial structures (Bilgin et al., 2007; Tabesh et al., 2007), and ensemble methods based on Support Vector Machines and Adaboost (Doyle et al., 2006b; Qureshi et al., 2008). An overview of these techniques and their applications is provided in (He et al., 2012; Gurcan et al., 2009; Veta et al., 2014). In this work, we focus only on deep learning-based techniques due to their recent and widespread success in computer vision.

Deep Learning (DL) models (Goodfellow et al., 2016), and in particular Convolutional Neural Networks (CNNs), provide state-of-the-art performance in many visual recognition applications such as image classification (Krizhevsky et al., 2012), object detection (Redmon et al., 2016) and segmentation (Dolz et al., 2018). These supervised learning architectures are trained end-to-end with large amounts of annotated (labeled) training data, so as to encode a hierarchy of discriminant image features. More recently, the potential of DL models has begun to be explored in assisted pathology diagnosis (Janowczyk and Madabhushi, 2016; Daisuke and Shumpei, 2018; Li and Ping, 2018). Given the growing availability of histology slides, DL models have not only been proposed for disease prediction (Hou et al., 2016; Li and Ping, 2018; Sheikhzadeh et al., 2016; Spanhol et al., 2016a; Xu et al., 2016), but also for related tasks like detection and segmentation of tumor regions within WSI (Kieffer et al., 2017; Mungle et al., 2017), scoring of immunostaining (Sheikhzadeh et al., 2016; Wang et al., 2015), cancer staging (Shah et al., 2017; Spanhol et al., 2016a), mitosis detection

(Chen et al., 2016; Cireşan et al., 2013; Roux et al., 2013), gland segmentation (Caie et al., 2014; Gertych et al., 2015; Sirinukunwattana et al., 2017), and detection and quantification of vascular invasion (Caicedo et al., 2011).

Natural and histological images differ substantially. In natural images, semantic objects typically follow a common shape structure (especially rigid objects). Compared to histological images, this makes it relatively easier to distinguish the target objects from the background, thereby facilitating learning and object localization. Furthermore, the colors/textures of target objects are typically different from the background. In contrast, while histological images follow a common biological structure with repetitive micro-patterns, the overall shape of the global target (cancerous) region might differ arbitrarily and significantly from one image to another, which makes their pattern difficult to learn, and hence to locate. Moreover, cancerous regions typically have visual appearances (colors and textures) that are quite similar to the surrounding tissues and normal regions, which makes them much more difficult to distinguish from the background.

DL techniques proposed to analyze histological images often require full supervision to address key tasks, such as classification, localization, and segmentation (Janowczyk and Madabhushi, 2016; Daisuke and Shumpei, 2018). Normally, learning to accurately localize regions of interest requires dense pixel-level annotations of images. In order to train a CNN for, e.g. pixel-wise localization of cancerous regions, one typically requires a large number of histology images with pixel-level labels to optimize the parameters of the model. Considering the size and complexity of such images, dense annotations of images come at a considerable cost and require highly trained experts. Outsourcing this task to standard workers such as Mechanical Turk Worker is not an option. As a result, histology datasets are often comprised of large images that are coarsely-annotated according to the diagnosis. Therefore, it is clear that training powerful DL models to predict the image class and the regions linked to this class *without* dense annotations is highly beneficial in histology image analysis. Moreover, such methods are often an application of different techniques that have been proposed for natural scene images.

In this paper, we focus on DL models that can be trained using data with image-level labels in order to classify a histological image, while yielding pixel-wise scores, thereby localizing the corresponding regions of interest within the image. Techniques for weakly supervised learning (WSL) are very promising for this purpose because they exploit unlabeled inputs, as well as coarse (group-level) or ambiguous labels, which alleviate the need for dense labels. In the general context of weakly supervised learning (Zhou, 2017), it is common to categorize the methods into three main types: (1) inexact supervision, where samples are given only coarse or group-level labels; (2) incomplete supervision, where only a small subset of training data has labels, although unlabeled data is abundant; and (3) ambiguous or inaccurate supervision, where labels may be incorrect/noisy. The inexact supervision scenario is relevant in this paper, where training datasets only require global image-level annotations. Under this scenario, powerful techniques for multiple-instance learning (MIL) (Carbonneau et al., 2018; Cheplygina et al., 2019; Wang et al., 2018; Zhou, 2004) are generally considered, where individual instance labels (e.g. image pixels, segments or patches) are not observable or do not belong to well-defined classes – training instances are grouped into sets (e.g. images), and supervision is only provided for sets of instances

While there has been different reviews of machine/deep learning models for medical image analysis, and in particular for analysis of histological slides (Janowczyk and Madabhushi, 2016; Kandemir and Hamprecht, 2015; Daisuke and Shumpei, 2018; Sudharshan et al., 2019; Litjens et al., 2017) and medical video analysis (Quellec et al., 2017), they are focused on fully supervised or semi-supervised learning scenarios (Litjens et al., 2017) for classification and segmentation. To our knowledge, this paper presents the first survey of deep WSL models for classification and pixel-wise localization of regions of interest in histology images. Most of the DL models in this survey rely on an MIL framework either explicitly, by using its formulation, or implicitly, by splitting the entire image into instances for learning.

Deep WSL techniques (Cheplygina et al., 2019; Zhou, 2017) also provide the advantage of *interpretability* (Zhang and Zhu, 2018). Despite the success of deep neural networks in many applications, they are often seen as black boxes that lack the ability to provide explanatory factors of their predic-

tions (Lipton, 2018; Marcus, 2018; 2001; Ribeiro et al., 2016; Samek et al., 2017). The transparency issue – the absence of clear explanatory factors of a model's decision – is a potential liability for ML models applied to medical image analysis (O'Neil, 2016). *Interpretable ML* (Doshi-Velez and Kim, 2017; Molnar et al., 2018) is an emerging branch of ML that aims to develop new techniques that can explain model decisions. Visual attention maps represent one such technique developed for *pixel-wise localization* of image regions used by a model to make its predictions (Zhang and Zhu, 2018). The deep WSL models investigated in this paper produce an attention map, where high magnitude responses correspond to image regions of interest, without the need for pixel-level annotation (Zhou et al., 2016). From a medical perspective, pixel-wise region localization can provide an accurate visual explanatory factor for the model's prediction of a cancer type, which is a highly desirable property in decision support systems. For instance, regions of interest can be further inspected by a pathologist if they indicate cancerous regions.

This paper provides a survey of state-of-the-art deep WSL models that are suitable for the identification of diseases (e.g. type of cancer) in whole slide histology images, and pixel-wise localization of regions of interest that correspond to the predicted disease. Given a dataset of globally-annotated training images, these models allow to simultaneously classify images while localizing the corresponding regions of interest. Two types of WSL approaches have been proposed in the literature that build attention maps to localize regions – (1) bottom-up approaches that use forward-pass information, either by spatial pooling of representations/scores, or by detecting class regions, and (2) top-down approaches that use backward information, and are inspired by human visual attention. Most of these methods do not rely on any prior knowledge on the nature of the images at hand.

The most relevant models are compared experimentally in terms of accuracy for image classification, pixel-wise localization of regions, and complexity on several public benchmark histology datasets for breast and colon cancer. Unfortunately, histology datasets with both image- and pixel-level labels are rare, and several benchmarks are private. In order to improve histological image benchmarks for large scale evaluations of WSL methods, we also propose a protocol to build WSL datasets from WSIs. Our deterministic code and the coordinates of sampled patches from the CAMELYON16 dataset are publicly available.

This survey is organized as follows. Sec. 2 provides some background on histology image production and analysis as well as key challenges. In Sec. 3, different models for deep weakly supervised localization are described and analyzed with histology image analysis in mind. Finally, Sec. 4 presents the experimental methodology for our comparative study (datasets, protocols and performance metrics), while Sec. 5 presents quantitative and qualitative results, interpretation, and future research directions.

2 Histological image analysis – background and challenges

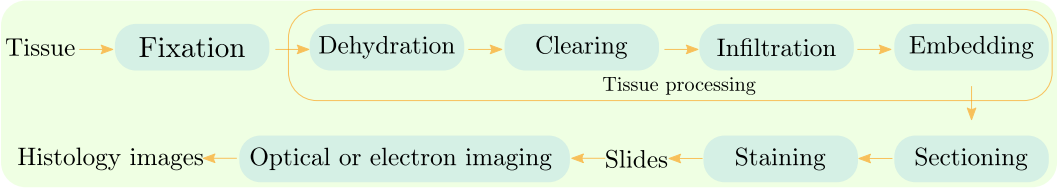

Figure 2: Histology tissue preparation and image production (He et al., 2010; 2012).

Histological analysis is performed by inspecting a thin slice (i.e. section) of tissue under an optical or electron microscope (Kiernan, 1990; Murphy and Davidson, 2001; Mescher, 2013; Gartner and Hiatt, 2006; Sternberg, 1997). The interpretation of histological images is considered as the gold standard for clinical diagnosis of cancer and identification of prognostic and therapeutic targets. Histopathology, the microscopic study of biopsies to locate and classify diseases, has roots in both clinical medicine and basic science (Sternberg, 1997). In this section, we first summarize the production of histological images, from tissue preparation to imaging technologies. Then, we briefly review histological image analysis, its relation to other types of medical imaging, and its main challenges.

2.1 IMAGE PRODUCTION:

Fig. 2 presents an overview of the process of obtaining histology images. Fixation is the first stage of preparation for subsequent procedures, which should be conducted in real time to preserve the samples as well as possible. Different fixatives (e.g. precipitant and crosslinking) or methods (e.g. heat fixation and immersion) may be used. For example, the precipitant fixatives (e.g. methanol, ethanol, acetone, and chloroform) dehydrate the tissue samples, removing lipids and reducing the solubility of proteins. After fixation, the tissue must be adequately supported, e.g. frozen or embedded in a solid mold, to allow sufficiently thin sections to be cut for microscopic examination. Common treatments employ a series of reagents to process the fixed tissue and embed it in a stable medium such as paraffin wax, plastic, or resin. Such treatments include the main steps of dehydration[1], clearing, infiltration, and embedding (Chandler and Roberson, 2009; Nelson et al., 2008; Wootton et al., 1995).

The embedded tissue sample is finally cut into thin sections (e.g. $5\mu m$ for light microscopy and $80 - 100nm$ for electron microscopy). The transparent sections are usually produced with a microtome, an apparatus feeding the hardened blocks through a blade with high precision. After cutting, the sections are floated in warm water to smooth out any wrinkles. Then, they are mounted (by heating or adhesives) on a glass slide. Once they are attached on the slide, the process is reversed prior to staining. The wax is removed with a solvent (usually xylenes) and the tissue is re-hydrated through a series of solutions in which the alcohol - water ratio is changed. The gradual rehydration preserves tissue architecture. Now, the sections are ready for staining, which helps to enhance the contrast and highlight specific intra- or extra-cellular structures. A variety of dyes and associated staining protocols are used. The routine stain for light microscopy is hematoxylin and eosin (H&E); other stains are referred to as special stains for specific diagnostic needs. Each dye binds to particular cellular structures, and the color response to a given stain can vary across tissue structures. For example, hematoxylin stains the nuclear components of cells dark blue and eosin stains the cytoplasmic organelles varying shades of pink, red, or orange. (Kiernan, 1990; Ross et al., 2003) provide a detailed description of common laboratory stains. After staining, the stained section on the slide is covered to protect the tissue and provide better visual quality for microscope examination.

After the tissue has been prepared, light microscope (Murphy and Davidson, 2001; Török and Kao, 2007) is used to take digital histology images of the stained sections. Additional details on different types of microscopes and image production are provided in (He et al., 2012; 2010).

2.2 IMAGE ANALYSIS:

In histology image analysis for cancer diagnosis, histopathologists visually inspect the regularities of cell shapes and tissue distributions. Such histopathological study has been extensively employed for cancer detection and grading applications, including prostate (Doyle et al., 2007; 2006a), breast (Basavanhally et al., 2008; Doyle et al., 2008), cervix (Guillaud et al., 2005; 2004), and lung (Jütting et al., 1999; Kayser et al., 2002) cancer grading, neuroblastoma categorization (Gurcan et al., 2006; Kong et al., 2007b), and follicular lymphoma grading (Cooper et al., 2009; Kong et al., 2007a).

Histopathology has attracted researchers from different disciplines including clinical medicine, biology, chemistry and machine learning. Computer-based image analysis has become an increasingly important field due to the high rate of production and the increasing reliance on these images by the biomedical community. Medical image processing and analysis in radiology (e.g. X-ray, ultrasound, CT, MRI) and cytology have been active research fields for several decades with numerous systems (Bankman, 2008; Greenberg, 1984; He, 2009; Yoo, 2004) and products[2][3][4] (Lamprecht et al., 2007; Schroeder et al., 2003) developed. However, the application of these systems in histology analysis is not straightforward due to the significant difference in the imaging techniques and image characteristics.

[1] The purpose of dehydration is to remove water so that the paraffin wax can infiltrate.

[2] ImageJ (https://rsbweb.nih.gov/ij).

[3] Medical Image Processing, Analysis and Visualization (https://mipav.cit.nih.gov) (MIPAV).

[4] CellProfiler: Cell Image Analysis Software (https://www.cellprofiler.org).

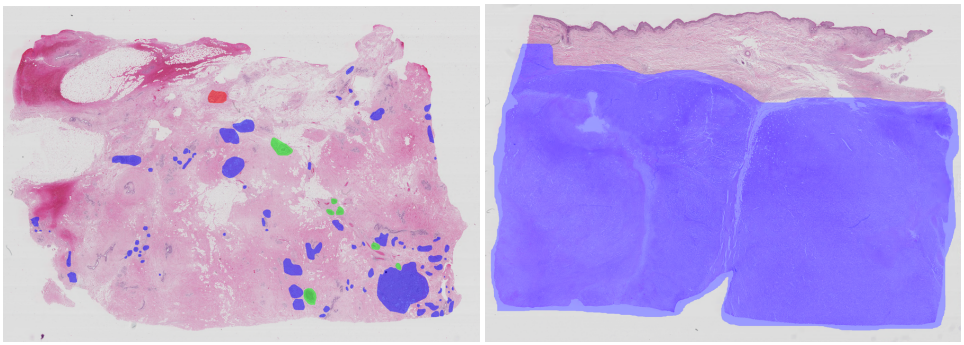

(a) (b)

Figure 3: Segmentation of two WSI from the ICIAR 2018 BACH Challenge. Colors represent cancerous regions of different types: red for `Benign`, green for `In Situ Carcinoma` and blue for `Invasive Carcinoma`. We can see an important differnece in the size and presence of regions (Aresta et al., 2018).

The complexity of histological images is defined by several factors including overlapping tissue types and cell boundaries and nuclei corrupted by noise; some structures, such as cell boundaries, may appear connected or blurred. These factors make it difficult to extract cell regions (e.g. nuclei and cytoplasm) by traditional image segmentation approaches. On the other hand, cytology images are taken at higher magnification level which results in clearly identified cell compartments. Computer-based histology analysis systems generally exploit a much larger quantity of image features to derive clinically meaningful information than similar systems for radiology and cytology (He et al., 2012). Nevertheless, the image analysis systems for these three domains generally consist of a common sequence of steps of image restoration, segmentation, feature extraction, and pattern classification.

2.3 Key challenges:

Recently, histological image analysis has attracted much attention in the ML and computer vision communities (Daisuke and Shumpei, 2018; Litjens et al., 2017; Spanhol et al., 2016a; Sudharshan et al., 2019) resulting in open competitions and public datasets such as GlaS (Sirinukunwattana et al., 2017), TUPAC16 (Veta et al., 2018), CAMELYON (Bándi et al., 2019; Ehteshami Bejnordi et al., 2017) and BACH 2018 (Aresta et al., 2018). The rest of this section describes the main difficulties of designing ML models for visual recognition using this type of images.

High resolution images Pathology images come often in high resolution (WSI, Fig. 3), leading to difficulties in terms of memory storage and processing time. A WSI has a higher resolution than the most common medical imaging types. For instance, the largest radiological image datasets obtained on a routine basis are high resolution chest CT scans comprising approximately $(512, 512, 512)$ spatial elements (~ 134 million voxels). In contrast, a single core of prostate biopsy tissue digitized at $40\times$ magnification is approximately $(15,000, 15,000)$ elements (~ 225 million pixels). To put this in context, a single prostate biopsy procedure can contain anywhere between 12 and 20 biopsy samples or approximately 2.5–4 billion pixels of data generated per patient study (Hipp et al., 2011; Gurcan et al., 2009). In practice, this issue is addressed either by downsampling to lower resolution WSI, which results in a significant loss of image details, or by preserving such details and losing the spatial information of the entire WSI by sampling patches from the WSI. A potential issue in sampling patches is that the WSI labels are not transferred correctly to the patch. A sampled patch from a WSI with a cancerous label may contain only healthy tissue, however, it will be assigned the class of the WSI. This inconsistency in patches labeling can mislead ML models during the training process and decrease the model's performance (Frenay and Verleysen, 2014; Sukhbaatar et al., 2014; Zhang et al., 2017). Moreover, the high resolution of WSI makes pixel-level annotation impractical and extremely time consuming. In practice, the WSI annotation is coarse and scarce (i.e. the overall

diagnosis) (Fig.3). This prevents from obtaining large corpora to accurately train ML models for pixel-wise localization and segmentation of images.

Heterogeneous data Another key challenge in histological image analysis is related to the heterogeneity of data due to variations in staining. As described in Sec. 2.1, histology images are produced after many processing steps. Since they involve different chemical processes, many variables may affect the resulting histology image stain including the target diagnosis, the operator, the laboratory, the type of used chemicals, the duration of exposure to them, the microscope, and many other factors. Fig. 4 shows an example of such stain variation. While it is easy for pathologists to discard these variations, ML models can be heavily and negatively affected since they are sensitive to changes in the statistics of input signals (Shimodaira, 2000; Sugiyama and Kawanabe, 2012), in particular neural based models (Szegedy et al., 2013). In practice, this issue can be alleviated either by performing color normalization (Ciompi et al., 2017; Janowczyk et al., 2017) or color augmentation during training to improve robustness to stain variations. Among these strategies, color augmentation[5] is particularly relevant when training using small datasets.

Noisy annotations Noisy or ambiguous annotations are a common practical issues in ML. In histological image analysis, this issue arises as a result of the way the pathologists grade WSIs. Often, such annotation is conducted by assigning the worst stage of cancer to the image. Therefore, a WSI that is labeled with a specific grade is more likely to contain most of the grades that are lower than the labeled grade. During the training of ML algorithms, sampling patches is a common strategy used to deal with large images. In this case, the WSI label is transferred to each patch. Such label transfer is not reliable and introduces noise and inconsistency in the patch label. Label inconsistency can degrade model performance and entangle learning (Frenay and Verleysen, 2014; Sukhbaatar et al., 2014; Zhang et al., 2017). Most of the time, a cancerous patch contains a relatively small cancerous region, while the rest is normal. The issue is aggravated when having many classes to characterize non-cancerous and cancerous lesions (e.g. `benign`, `in situ`, `invasive` along with the `normal` class).

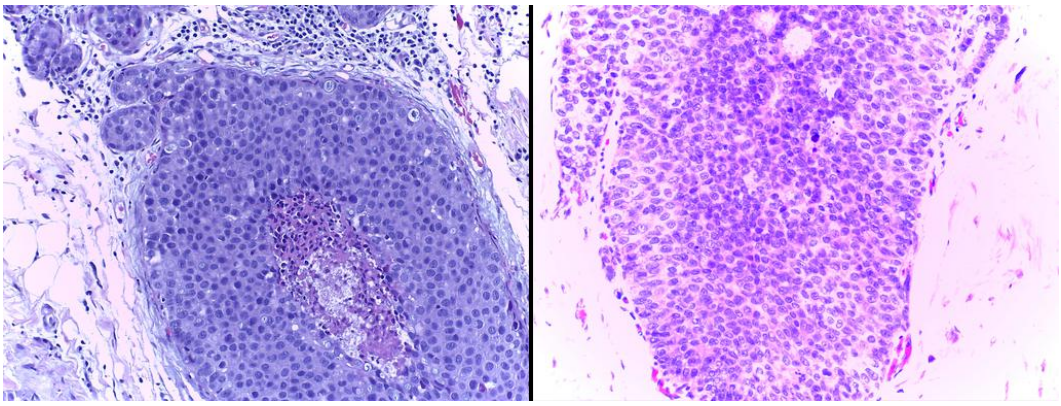

Figure 4: Difference in staining for two images labeled both as *In Situ Carcinoma* extracted from different WSI (Aresta et al., 2018).

3 A survey of deep weakly supervised learning models for classification and localization

This section presents a review of state-of-the-art deep WSL models that can be *simultaneously* trained to perform two tasks – image classification and pixel-wise localization – using only WSIs that are annotated with global labels. Most of these techniques have been originally proposed to process natural images and validated on well-known public benchmarks such as ImageNet (Deng et al., 2009),

[5] e.g. randomly modifying brightness, contrast, saturation and hue within chosen ranges

Pascal VOC (Everingham et al., 2010) and MS-COCO (Lin et al., 2014). We first present an overall taxonomy of techniques for deep WSL in natural images, and then describe the models that are most relevant for our application. We end this section with a critical analysis, and a selection of relevant models for experimental evaluation of histological datasets (Sec. 3.4).

3.1 Overall taxonomy:

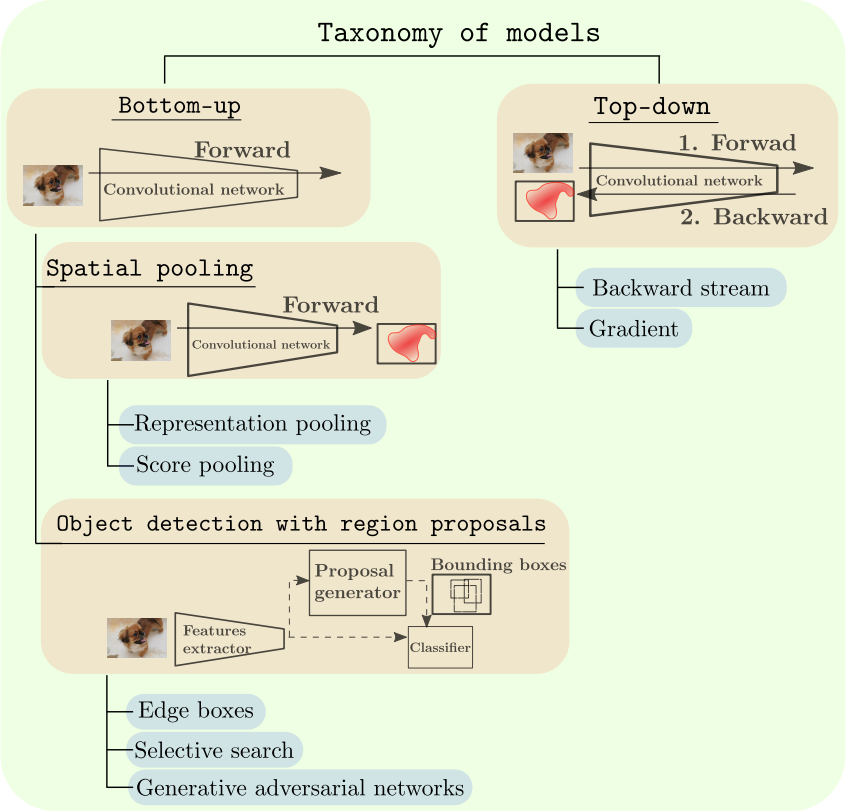

Figure 5: Overall taxonomy of deep WSL models that allow for classification and localization based on global image annotations.

Among deep weakly supervised localization methods, we identify two main categories based on the way region localization is achieved (Fig. 6): bottom-up methods that are based on the forward pass information within a network, and top-down methods that are based on the backward information. Fig. 5 illustrates the overall taxonomy. All these methods employ **a localization mechanism** in order to isolate regions of interest. They rely either on: (1) an attention map where high magnitude responses correspond to salient regions within the image – i.e. regions of interest – or (2) a bounding box that encloses the region of interest. These methods also require **image-level annotation** in order to train DL model to classify an image while localizing the corresponding regions of interest within the image.

3.1.1 Bottom-up weakly supervised localization techniques:

With these methods, the pixel-wise localization is based on the activation of the feature maps resulting from the standard flow of information within a network from the input signal into the output target (forward pass, Fig. 6 (*top*)). Within this category, we identify two different subcategories of techniques to address weakly supervised localization. The first category contains techniques that are based on spatial pooling of either representations or scores which aim at classifying a bag of instances while obtaining localization throughout the activation of the spatial maps (i.e. classifying instances). The

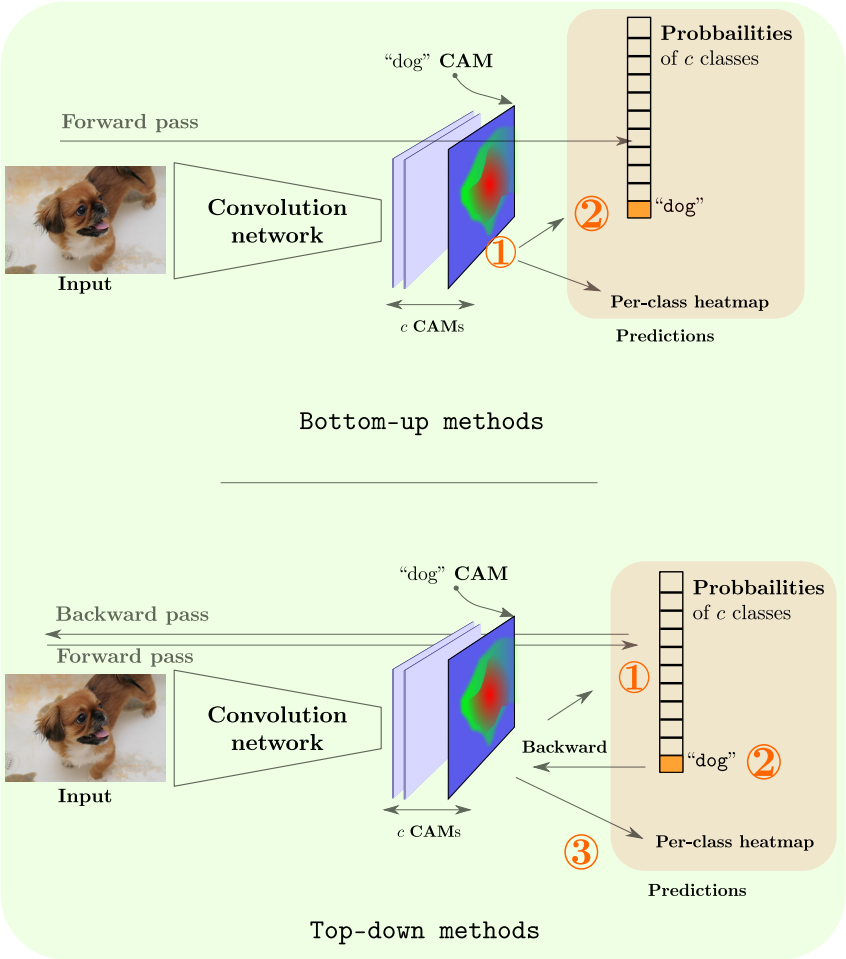

Figure 6: An illustration of the main difference between bottom-up (*top*) and top-down (*bottom*) WSL techniques. Both approaches provide CAMs. However, bottom-up techniques produce them during the forward pass, while top-down techniques require a forward, then a backward pass to obtain them.

second category contains techniques related to object detection which essentially aim to localize regions associated with classes.

Methods based on spatial pooling. This category of techniques are mainly based on learning a spatial representation that promotes the localization of the regions of interest, which is later pooled to classify the input. Within this category, we distinguish two main strategies which can both be encapsulated within MIL framework. The first approach aims at finding a bag representation based on each representation of local patches (i.e., instances), while the second approach scores the entire bag based on local scores of instances (regions). In both cases, such spatial local scoring can be used as a indicator of the presence/absence of the corresponding class. Hence, given image data with global annotations, these WSL models enable to obtain relatively accurate pixel-wise maps for localization, thereby surpassing the need for pixel-wise annotation.

• The first approach aims at building a global representation of the input and then classify it. This corresponds to the approach initially proposed by (Zhou et al., 2016) in which the global representation is obtained by averaging the local representations. The class-specific activations are then obtained by a linear combination of the features using the weights of the classification layer. This strategy has been widely used for natural scene images as well as for medical images (Feng et al., 2017; Gondal et al., 2017; Izadyyazdanabadi et al., 2018; Sedai et al., 2018) where it often combines features from multiple levels (corresponding to different scales) to improve the performance. A more recent strategy

proposed by (Ilse et al., 2018) builds a representation as a weighted sum of the local representation where the weights are attention scores produced by a scoring function. • The second approach aims at obtaining a global score for each class based on the local scores. The classification is done at the instance level and the scores are pooled using different strategies. The first approach proposed by (Oquab et al., 2015) uses max pooling to obtain a score for the image, while the final score for a class is the maximum score of all the instances. However, this pooling technique tends to focus on small discriminative parts of objects (Zhou et al., 2016). To alleviate this problem, Pinheiro and Collobert (2015b) propose to use a smoothed approximation of the max function to discover larger parts of the objects of interest. Finally, (Durand et al., 2017; 2016) propose to use negative evidence to obtain a global score: instead of using only the maximum scoring instances, the pooling is based on both the maximum and minimum scoring instances which provides a strong regularization during training. This method has also been used in the medical field for histological image classification (Couture et al., 2018) and weakly supervised region localization and image classification in the same type of images (Courtiol et al., 2018).

Methods based on object detection. The second type of techniques within this category are related to Weakly Supervised Object Detectors (WSOD). The main goal of WSOD is to produce a region (or a set of regions) that are characteristic of one class (or a set of classes, not necessarily different). These regions are defined by rectangular bounding boxes and try to fit the object as much as possible (i.e. the bounding box is in contact with the outer edges of the object). The main difficulty of WSOD is to obtain an accurate placement of the bounding boxes. Most approaches rely on Region Proposal (RP) mechanisms such as Edge Boxes (EB) (Zitnick and Dollár, 2014) or Selective Search (SS) (Uijlings et al., 2013; Van de Sande et al., 2011). The RP mechanism is used to generate a list of candidate regions that are likely to contain an object of interest. It can be introduced at different levels of the architecture and it was shown to heavily impact the performance of the overall algorithm. An early approach using this mechanism is used in (Teh et al., 2016) where the content of each region is passed through attention and then scoring modules to obtain an average image feature which is a weighted average of the proposals. Bilen and Vedaldi (2016) propose a WSOD framework to address the task of multi-class object detection. More improvements of this work have been proposed since then (Kantorov et al., 2016; Tang et al., 2017). Other approaches use multi-step training to first train a CNN for localization and then refine it for object detection (Diba et al., 2017; Ge et al., 2018; Sun et al., 2016). Wan et al. (2018) propose to train a network to reduce its variance in terms of the proposals by reducing an entropy defined over the position of the proposals. Shen et al. (2018) propose to use generative adversarial networks to generate the proposals.

3.1.2 Top-down weakly supervised localization techniques:

This second main category is based essentially on the backward pass information within a network to build an attention map in order to localize regions with respect to a selected class. The main idea in this category is based on an optimization algorithm that aims at maximizing the posterior response of the network given an output target (i.e. class). This optimization scheme allows building an activation map where neurons that support the output target are activated. Different approaches have been used to build these activation maps including a probabilistic Winner-Take-All process that combines bottom-up and top-down information to compute the winning probability of each neuron (Zhang et al., 2018a), a backward layer (Cao et al., 2015), or by computing the gradient of the output target with respect to the feature maps (Chattopadhyay et al., 2018; Selvaraju et al., 2017). In practice, these approaches are known to be computationally expensive.

3.2 Description of bottom-up techniques:

Let us consider a set of training samples $\mathbb{D} = \{(\mathbf{x}^{(t)}, y^{(t)})\}$ of images $\mathbf{x}^{(t)} \in \mathbb{R}^{D \times H^{\text{in}} \times W^{\text{in}}}$ with H^{in}, W^{in} and D being the height, width and depth of the input image respectively; and its image-level label (i.e. class) is $y^{(t)} \in \mathcal{Y}$ with C possible classes. For simplicity, we refer to the input and its label as $(\mathbf{x}, y)$.

The training procedure aims at learning a neural network that models the function $f_{\boldsymbol{\theta}} : \mathbb{R}^{D \times H^{\text{in}} \times W^{\text{in}}} \rightarrow \mathcal{Y}$ where the input $\mathbf{x}$ has an arbitrary height and width and $\boldsymbol{\theta}$ is the network

parameters. Typically, in a multi-class scenario, given an input, the network outputs a vector of scores $\boldsymbol{s} \in \mathbb{R}^C$ which is then normalized to obtain a posterior probability using a $\mathrm{softmax}$ function,

$$\Pr(y = i|\mathbf{x}) = \mathrm{softmax}(\boldsymbol{s})_i = \frac{\exp(\boldsymbol{s}_i)}{\sum_{j=1}^{C} \exp(\boldsymbol{s}_j)} \ . \tag{1}$$

The predicted class is the one corresponding to the index of the maximum probability which is equivalent to taking the argmax of the score vector: $\underset{i}{\mathrm{argmax}} \Pr(y = i|\mathbf{x}) = \underset{i}{\mathrm{argmax}}\, \boldsymbol{s}_i$.

Beside the classification of the input image, we are also interested in the pixel-wise localization of the region of interest within the image. The network can also output either a region of interest r related to the predicted class or a set of regions $\mathbb{R}_{\text{inter}} = \{r_i \mid i = 1, \ldots, t\}$, as well a set of C activation maps of height H and width W to indicate the location of the regions of each class. We note this set as a tensor of shape $\mathbf{M} \in \mathbb{R}^{C \times H \times W}$; where $\mathbf{M}_c$ indicates the c^{th} map. $\mathbf{M}$ is commonly referred to as *Class Activation Maps* (CAM). In most practical cases, the height and the width of the CAM is *smaller* than the height and the width of the input image by a factor S called stride such that $H = H^{\text{in}}/S$ and $W = W^{\text{in}}/S$.

3.2.1 Spatial pooling:

In this category, the beginning of the pipeline is usually the same for all techniques: a CNN extracts K feature maps $\mathbf{F} \in \mathbb{R}^{K \times H \times W}$, where K is the number of feature maps which is architecture-dependent. The feature maps $\mathbf{F}$ are then used to compute a score per class using a spatial pooling either on the representation or the scores of the instances.

We can distinguish two main approaches to compute the per-class score: spatial representation pooling and spatial score pooling.

Spatial representation pooling. In this first approach, the feature maps produced by the CNN are spatially pooled to form a single representation $\boldsymbol{f} \in \mathbb{R}^K$ of the whole input which is then classified.
Global average pooling (GAP). Lin et al. (2013) propose a way of regularizing neural networks by adding GAP layers to avoid the use of fully connected layers that dramatically increase the number of parameters. The GAP module allows to obtain dense features $\boldsymbol{f} \in \mathbb{R}^K$ based on spatial features $\mathbf{F} \in \mathbb{R}^{K \times H \times W}$ by averaging the activations of each map,

$$\boldsymbol{f}_k = \frac{1}{H\,W} \sum_{i=1,j=1}^{H,W} \mathbf{F}_{k,i,j} \ , \tag{2}$$

where $\boldsymbol{f}_k$ is the k^{th} feature of the output of the GAP. Zhou et al. (2016) show that this pooling strategy can be used to obtain a localization ability in a CNN using only global labels. Typically, in a CNN, the last layer which classifies the representation $\boldsymbol{f}$ is a fully connected layer parametrized by $\boldsymbol{W} \in \mathbb{R}^{C \times K}$ such that $\boldsymbol{s} = \boldsymbol{W}\boldsymbol{f}$ (bias is omitted for simplicity). The CAMs, denoted as $\mathbf{M} \in \mathbb{R}^{C \times H \times W}$ are then obtained using a weighted sum of the spatial feature $\mathbf{F}$,

$$\mathbf{M}_c = \sum_{k=1}^{K} \boldsymbol{W}_{c,k}\, \mathbf{F}_k \ . \tag{3}$$

The main advantage of Eq. 3 is that it does not depend on the size of the input. This technique has been used extensively in medical domain (Feng et al., 2017; Gondal et al., 2017; Izadyyazdanabadi et al., 2018; Sedai et al., 2018), often combined with a multi-level feature maps. Combining feature maps from lower layers within the network can allow to obtain CAM with high resolution and more precision. (Zhu et al., 2017) propose soft proposal networks (SPNs) which are based on (Zhou et al., 2016) with an extra module that generates a proposal map which highlights regions of the object in hand. Such proposal map is generated iteratively using random walk over a fully connected directed graph that connects each position within a feature map at a specific convolution layer. (Zhu et al., 2017) can be also categorized as an object detection method with region proposals (Sec. 3.2.2).
(Zhang et al., 2018b) propose to build the CAMs $\mathbf{M}$ by taking the maximum between two set of CAMs. The first set of CAMs is obtained in the same way as in (Zhou, 2017) and used to mask (or

erase) a part of the feature maps based on thresholding. Using these masked features, a second set of CAMs is computed using a different layer. (Zhang et al., 2018b) argue that it makes a CNN discover relevant regions more effectively.

Attention-based deep MIL. Ilse et al. (2018) propose to build an image (i.e. bag) representation using a weighted average of the instances representations based on an attention mechanism (Bahdanau et al., 2015). Given a set of features $\mathbf{F} \in \mathbb{R}^{K \times H \times W}$ extracted for an image, the representation $\boldsymbol{f}$ of the image is computed as,

$$\boldsymbol{f} = \sum_{i=1,j=1}^{H,W} \boldsymbol{A}_{i,j} \mathbf{F}_{i,j} \ , \tag{4}$$

$$\text{and} \quad \boldsymbol{A}_{i,j} = \frac{\exp(\psi(\mathbf{F}_{i,j}))}{\sum_{i=1,j=1}^{H,W} \exp(\psi(\mathbf{F}_{i,j}))} \ ,$$

Where $\mathbf{F}_{i,j}$ is (by an abuse of notation) the feature vector of the location (i.e. instance) indexed by i and j. $\psi : \mathbb{R}^K \to \mathbb{R}$ is a scoring function. The resulting representation $\boldsymbol{f}$ is then classified by a fully connected layer. Ilse et al. (2018) propose two scoring functions,

$$\psi_1(\boldsymbol{f}) = \boldsymbol{w} \tanh(\boldsymbol{V}\boldsymbol{f}) \ , \tag{5}$$

$$\psi_2(\boldsymbol{f}) = \boldsymbol{w}\big[\tanh(\boldsymbol{V}\boldsymbol{f}) \odot \sigma(\boldsymbol{U}\boldsymbol{f})\big] \ , \tag{6}$$

where $\boldsymbol{w} \in \mathbb{R}^L$ and $(\boldsymbol{V}, \boldsymbol{U}) \in \mathbb{R}^{L \times K}$ are learnable weights. This approach is designed specifically for binary classification and produces a matrix of attention weights $\boldsymbol{A} \in [0,1]^{H \times W}$ with $\sum \boldsymbol{A} = 1$. This means that for a positive bag, negative instances should have an attention weight close to 0 while positive instances should have a high attention weights. However, it is not possible to determine if an instance is actually predicted as positive or not except by fixing a threshold.

Spatial score pooling. In this second approach, the feature maps are used to produce the CAMs directly by classifying each instance. Then, the global per-class scores are obtained by pooling the instances' scores. The methods mainly differ by their strategy used to pool the instances' scores.

First, it is important to note that GAP (Zhou et al., 2016) is designed to be used when the last classification layer of a model is linear. The consequence is that the pooling can also be done on scores which is equivalent. With GAP, Eq. 2, and Eq. 3 allow to compute the per-class scores $\boldsymbol{s}_c$ as,

$$\begin{aligned} \boldsymbol{s}_c &= \sum_{k=1}^{K} \boldsymbol{W}_{c,k} \boldsymbol{f}_k \ , \\ &= \frac{1}{H\,W} \sum_{k=1}^{K} \boldsymbol{W}_{c,k} \sum_{i=1,j=1}^{H,W} \mathbf{F}_{k,i,j} \ , \\ &= \frac{1}{H\,W} \sum_{i=1,j=1}^{H,W} \mathbf{M}_{c,i,j} \ . \end{aligned} \tag{7}$$

Eq. 7 shows that the per-class score is computed by averaging the activations of the corresponding CAM. Instead of averaging the feature maps, taking the maximum value can be considered as well (Oquab et al., 2015). However, such an operation tends to favor small discriminative regions (Zhou et al., 2016). (Pinheiro and Collobert, 2015a; Sun et al., 2016) consider using an approximation to the maximum function (Boyd and Vandenberghe, 2004) as an alternative where the score of each map can be computed as,

$$\boldsymbol{s}_c = \frac{1}{q} \log\Big[\frac{1}{H\,W} \sum_{i=1,j=1}^{H,W} \exp(q\,\mathbf{M}_{c,i,j})\Big] \ , \tag{8}$$

where $q \in \mathbb{R}_+^*$ controls the smoothness of the approximation. A smaller value of q makes the approximation closer to the average function while a larger q makes it close to the maximum function. Thus, small values of q make the network consider large regions while large values consider only small regions.

Negative evidence mixing. Durand et al. (2017; 2016) compute m feature maps per-class using 1×1 convolution. Then, compute their average to obtain one feature map. While standard pooling methods are based on considering the maximum or the average of the activations within a map, (Durand et al., 2017; 2016) consider using both maximum and minimum activations. A maximum activation indicates a positive evidence of the presence of the corresponding object. In the other hand, a minimum activation indicates a negative evidence (Durand et al., 2015) of its presence. The benefits of such mixing of both information provides a regularization mechanism that prevents the model from overfitting compared to learning only from maximum activation for instance (Durand et al., 2017; 2016). Such pooling is computed over each map by considering the sum of the average of n^+ maximum activation and n^- of minimum activation. Specifically, the score for each class is computed as,

$$\boldsymbol{s}_c = \frac{Z_c^+}{n^+} + \alpha \frac{Z_c^-}{n^-} \,, \tag{9}$$

where Z_c^+ and Z_c^- correspond to the sum of the n^+ highest and n^- lowest activations of $\mathbf{M}_c$ respectively and α is a hyper-parameter that controls the importance of the minimum scoring regions. Such an operation consists in selecting for each class the n^+ highest activation and the n^- lowest activation within the corresponding map. In medical domain, Courtiol et al. (2018) show the benefit of using negative evidence.

3.2.2 Object detection with region proposals:

The second category of techniques relevant for weakly supervised localization is related to object detection. Many techniques have been proposed in order to find the coordinates of a relevant region using only image-level labels. The pipeline of these detectors usually contains three operations presented in Fig. 7. The order of the operations of this pipeline can be changed to accommodate different strategies of supervision but the principle of the operations remains the same. In the next paragraphs, we describe some of the related work that is based on WSOD.

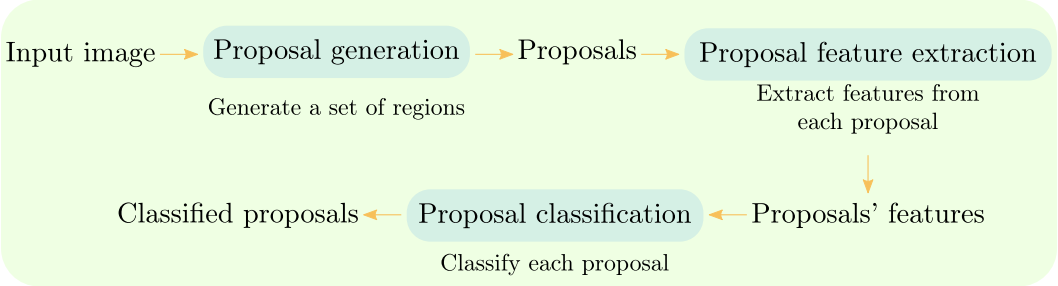

Figure 7: Standard pipeline for WSOD methods.

Attention networks for WSOD. In a similar manner to (Ilse et al., 2018), Teh et al. (2016) propose to use a fully connected network to generate attention score for each instance. The initial region proposals are generated using the Edge Boxes (EB) (Zitnick and Dollár, 2014) on the input image. Then for each region, a feature vector representation is extracted using a pre-trained CNN. A fully connected network produces a score for each feature vector, which is normalized using a $\mathrm{softmax}$ operation on the proposals. The image representation is the weighted sum of the feature vectors by the attention weights. The resulting representation is then classified by a fully connected layer. Bency et al. (2016) propose an efficient way to extract top scoring regions from a CNN by performing a tree search on sub-regions of the feature maps. Given the feature maps produced by a CNN, four children regions of small size are extracted and each region is interpolated to produce a feature map of the same size as the parent. These four regions are classified by a fully connected layer. The top-scoring region for the class of the image then becomes the parent region. This process is iterated until it converges to a region with the maximum probability for the class of the image at train time.

Weakly supervised deep detection networks (WSDDN). (Bilen and Vedaldi, 2016) is one of the approaches that has achieved an important improvement compared to previous WSOD techniques

(Bilen et al., 2015; 2014; Cinbis et al., 2017; Wang et al., 2014). Bilen and Vedaldi (2016) propose a modified CNN architecture with two streams: one focusing on recognition and the other one on localization. In this approach, the proposals are generated from the input image using Selective Search (SS) (Uijlings et al., 2013; Van de Sande et al., 2011) or Edge Boxes (EB). In parallel, a CNN produces feature maps for the input image. A Spatial Pyramid Pooling (SPP) (He et al., 2014) is then used to extract the features corresponding to the region proposals from the feature maps. At this point, each region's features are processed by two different fully connected networks to produce classification scores $\boldsymbol{S}^{\text{class}} \in \mathbb{R}^{|\mathbb{R}_{\text{inter}}| \times C}$ and detection scores $\boldsymbol{S}^{\text{det}} \in \mathbb{R}^{|\mathbb{R}_{\text{inter}}| \times C}$. These scores are then normalized to obtain $\boldsymbol{\sigma}^{\text{class}}$ and $\boldsymbol{\sigma}^{\text{class}}$ using a $\mathrm{softmax}$ function,

$$\boldsymbol{\sigma}^{\text{class}}_{i,c} = \frac{\exp \boldsymbol{S}^{\text{class}}_{i,c}}{\sum_{j=1}^{C} \exp \boldsymbol{S}^{\text{class}}_{i,j}} , \tag{10}$$

$$\boldsymbol{\sigma}^{\text{det}}_{i,c} = \frac{\exp \boldsymbol{S}^{\text{det}}_{i,c}}{\sum_{j=1}^{C} \exp \boldsymbol{S}^{\text{det}}_{i,j}} . \tag{11}$$

The final region-level scores $\boldsymbol{R} \in \mathbb{R}^{|\mathbb{R}_{\text{inter}}| \times C}$ are obtained throughout an element-wise product of the normalized classification and detection scores, and the per-class image-level scores are obtained by summing the region-level score for each class,

$$\boldsymbol{R} = \sigma^{\text{class}} \odot \sigma^{\text{detect}} , \tag{12}$$

$$\text{and} \quad \boldsymbol{s}_c = \sum_{i=1}^{|\mathbb{R}_{\text{inter}}|} \boldsymbol{R}_{i,c} . \tag{13}$$

(Kantorov et al., 2016) further improve this approach by adding more context information where $\boldsymbol{S}^{\text{det}}$ becomes the combination of the score of a region and its surrounding (i.e. spatial context). This allows to obtain a better discrimination of the proposed region, eliminating regions that do not tightly fit an object.

Online instance classifier refinement. Tang et al. (2017) propose another improvement of the WSDDN by refining the proposals multiple times based on the overlap of the proposals. When a proposal is a top-scoring region for a class that is present in the image, the refinement algorithm will look for all the other proposals that have a high overlap with it and set their label to one for this class. This process forces the model to gradually detect larger parts of objects as the training advances by fusing on high scoring and overlapping regions.

Weakly supervised region proposal network and object detection. Tang et al. (2018) suggest that the proposal generation has a great influence on WSOD performance and can benefit from the feature maps produced by a CNN instead of simply using SS or EB on the input image. Once the feature maps are obtained from the CNN, the proposals are generated in three steps. The first proposals are generated using a sliding window on the image. They are refined using the same principle as EB method. To further refine them, a fully connected network re-evaluates the objectness of the refined proposals. Finally, the different proposals are classified by extracting a feature vector representation using the same *region of interest* pooling algorithm as in Fast R-CNN (Girshick, 2015). This method presents the advantage of not relying on SS nor EB to generate the proposals which are known to be computationally expensive.

Region proposal filtering using top-down stream for multi-label recognition. Ge et al. (2018) propose to use multiple sources of information to obtain CAMs for better object detection. In this technique, the authors combine object heatmaps with top-down attention maps to obtain more accurate object instances. The object heatmaps are obtained using a pre-trained CNN, by adding the class probabilities of each proposal to its corresponding pixels when the class is present in the image. The attention maps are obtained using excitation backprop (Zhang et al., 2018a) on a second pre-trained CNN. Object heatmaps obtained in a feedforward manner are usually too smooth to give precise information on the object boundaries. Combining them with attention maps allows to better filter the region proposals, and reduce the number of false positive regions.

Deep self-taught learning. Jie et al. (2017) suggest that training detectors with image-level supervision leads to poor-quality positive proposals. To start from good proposals, the authors propose to use a

graph-based approach to refine the proposals initially generated by EB, by finding the dense sub-graph of proposals based on their spatial overlap. To improve the quality of the proposals, they propose to train a detector by *iteratively* selecting high-quality proposals based on their relative improvement compared to the previous training epoch. With this self-supervision, low-quality proposals obtain low improvement over the epochs, contrary to high-quality ones. This allows the detector to select high-quality regions.

Min-entropy latent model for WSOD. Wan et al. (2018) suggest that there is an inconsistency between the weak supervision (absence of labels of object localization) and the learned objectives (i.e. asking the model to learn the object location) which introduces randomness and uncertainty to object locations and object detectors. In order to decrease such uncertainty, the authors propose to minimize the entropy of a latent model which aims to reduce the variance of the proposals (i.e. the locations of the objects). The proposals are initially generated by SS and a feature representation is extracted for each proposal. They are further refined using a graph-based approach to fuse them when they present the high confidences for a class and a significant spatial overlap. Then, the model is trained to minimize the classification error on the most confident proposals. This produces sparse predictions on the most confident proposals which reduces the randomness of selected proposals during learning.

Generative adversarial networks for WSOD. A main criticism of the WSOD techniques is that they usually follow a multi-step pipeline (Fig. 7), leading to expensive computational cost, hence, a slow running time. Shen et al. (2018) propose to improve the speed by training a WSOD within a generative adversarial framework. Three models are used in this approach: a generator G which is a one-stage detector (Liu et al., 2016) that outputs bounding boxes with associated probabilities, a discriminator D predicting the quality of bounding boxes for an image, and a surrogator F which is a modified version of WSDDN used to estimate image proposals. The intuition is that G, which is fast, will learn to generate the same proposals as F, which is slow in comparison, with the supervision of D. D learns to distinguish bounding boxes generated by G from accurate estimated ones generated by F.

Table 1: Main advantages and drawbacks of different types of deep WSL models.

Methods	Advantages	Limitations
Bottom-up	• easy to implement • more popular in the community	–
Top-down	• can be used to interrogate the network about any given label in a more principled way • can provide CAMs at each layer • a generalization to CAM methods	• complex and difficult to implement • less common • computationally expensive during train/inference (run-time, memory scale with the size of the image)
Bottom-up: Spatial pooling	• fast training/inference • provide heatmaps to delimit unstructured objects • do not rely on priors on the images • can provide pixel-wise delimitation (more precise compared to bounding boxes)	• heatmaps cover minimal region of the object of interest (blobs, less precise) • heatmaps require interpolation to fit the image size (loss of precision)
Bottom-up: Object detection	• provide bounding boxes • often, designed with priors on the image (contours, homogeneity) • can deal intrinsically with multi-instance	• computationally expensive/slow (training/inference) • bounding boxes are unable to delimit unstructured objects • bounding boxes provide a rough localization (less precise)

3.3 Description of top-down techniques:

In this second main category, the weakly supervised pixel-wise localization is determined based on information obtained from the stream that goes from the output (top) toward the input (down). We can distinguish two related methods: backward based-methods, and gradient based-methods. We note that such approaches are computationally expensive compared to bottom-up methods (Sec. 3.2).

Backward stream based-methods. Excitation backprop for top-down attention (Zhang et al., 2018a) is one of the illustrative examples of such approach. In its formulation, the authors propose a probabilistic winner-take-all formulation in the backward pass of the model to determine which units are active with respect to a selected output class. By defining a prior distribution over the output

classes, the winner neurons of lower layers can be sampled recursively in a top-down fashion. Given a neuron a_z at some layer, its probability can be determined using the probability of its parent neurons $a_t \in \mathbb{P}_z$ at the previous layer as follows,

$$\Pr(a_z) = \sum_{a_t \in \mathbb{P}_z} \Pr(a_z|a_t) \Pr(a_t) \ , \tag{14}$$

where $\Pr(a_z|a_t)$ is simply a normalized energy that flows from the neuron a_z to a_t with respect to all the neurons that share the same parent as a_z. Using such approach, it is possible to obtain a CAM at each convolutional layer. Since an image may contain many objects, the dominant neurons may belong to different classes. Thus, a CAM may contain the activations of more than one object. To deal with this, Zhang et al. (2018a) propose a *contrastive* attention that builds a highly discriminative CAMs by keeping only one class and suppressing the rest. Cao et al. (2015) propose a related work where an attention map is built with respect to a selected class using the backward information throughout a *feedback layer*. Neurons in feedback layers are updated iteratively to maximize the confidence of the output target. The selectivity in such neurons is controlled using a binary mask obtained throughout an optimization procedure.

Gradient based-methods. These approaches are based on computing the gradient of any output target with respect to the feature maps to determine the main locations that contribute to the prediction of the selected target. Such approaches are mainly used as *visual tools* to explain a network's decision. (Selvaraju et al., 2017) is an illustrative example of this approach. In order to compute the CAMs, the authors propose to use GAP (Eq. 3), where the coefficient of each feature map is computed using the gradient of the score of the selected target class with respect to that map. Therefore, a CAM for the class c is a linear combination of the feature maps, similar to Eq. 3,

$$\mathbf{M}_c = \text{ReLU}\left(\sum_{k=1}^{K} \boldsymbol{A}_{c,k}\ \mathbf{F}_k\right) , \tag{15}$$

$$\text{where} \quad \boldsymbol{A}_{c,k} = \frac{1}{H\,W} \sum_{i=1,j=1}^{H,W} \frac{\partial \boldsymbol{s}_c}{\partial \mathbf{F}_{k,i,j}} \ , \tag{16}$$

where $\boldsymbol{s}_c$ is the score for class c. This approach is a generalization of the the method proposed by (Zhou et al., 2016) where the derivative of the score with respect to the feature map is used. In the case where the last classification is linear, both formulation are equivalent. This approach has been improved in (Chattopadhyay et al., 2018) to obtain better localization, as well as explaining occurrences of multiple instances in a single image.

3.4 A CRITICAL ANALYSIS:

Our first observation is that all deep weakly supervised localization methods have been proposed and validated on natural images. Their application on histology images can be problematic due to the heterogeneous nature of these images. The second observation is that bottom-up techniques have attracted much more attention compared to top-down methods. A possible explanation to this is the simplicity of bottom-up methods which follows classical flow of information within a neural network. In contrast, top-down methods, which are inspired from human visual attention, are more complex in terms of implementation and inference. Moreover, they can be computationally expensive, more so when the size of the image is large. For these reasons, most of the techniques selected for our experimental evaluation are mainly from the bottom-up family.

Among bottom-up methods, we find weakly supervised localization methods based on a spatial pooling, allowing to locate regions after being trained using only global labels. Often, this category of techniques is straightforward to use on histological images, and does not rely on prior knowledge on the nature of the image at hand. Among the spatial pooling methods, we evaluate the work in (Zhou et al., 2016) which has shown promising results in terms of classification and weak localization. We consider using different pooling techniques: average pooling, max pooling, and log-sum-exponential pooling (LSE) (Eq. 8), along with Weakly supervIsed Learning of Deep Convolutional neurAl

neTworks (WILDCAT) pooling (Durand et al., 2017), which has shown interesting results in terms of classification and pixel-wise localization, and deep multi-instance learning (Deep MIL) (Ilse et al., 2018). All these methods have shown great potential for localization regions of interest while maintaining high levels of classification accuracy. The major drawback of these methods is that the resolution of the CAMs is limited due the stride of the backbone network used to extract features. When pixel-level evaluation is required (typically to evaluate the Dice index), we interpolate the CAMs to match the input size.

The Deep MIL method proposed in (Ilse et al., 2018) has two major limitations. Firstly, it is restricted to binary classification. Therefore, for datasets with more than two classes, we adapt this method by replicating the pooling and scoring module to match the number of predicted classes. Secondly, this method produces attention scores for each instance which sum to 1. When we evaluate at pixel-level, an instance is therefore predicted as belonging to the positive class if its attention weight is superior to $\frac{1}{HW}$. We acknowledge that this is not a perfect criterion as edge cases are not covered – if all instances are predicted with the same score, all attention weights are equal to $\frac{1}{HW}$ which does not indicate whether the initial score was high (positive instance) or low (negative instance). However, we have observed that this works well in practice, and allows showing the potential of this method.

In the bottom-up category, we also find WSOD techniques based on region proposals, mostly used for object detection. For our experiments, the approach in (Tang et al., 2018) is considered because it provides large improvements compared to other WSOD methods, and (Bilen and Vedaldi, 2016) which limits the use of SS or EB methods which are known to be computationally expensive. The main limitation presented in WSOD methods is that they are tailored to natural scene images. Therefore, most of them encode in their algorithms some priors on the object in such images. We recall that objects within natural scene images usually have a standard structure/shape, and they tend to be smooth; while a *cancerous region* within histological images, for instance, does not have any prior structure nor appearance. As a consequence of such adaptation for natural scene images, region proposal methods such as SS and EB rely on the fact that edges are likely to delimit an object and pixels inside an object are more likely to be similar. In histology images, the first fact is not clear to be true. Moreover, edges are expected to be very noisy due to high variation in the texture of the microscopic tissue and intensive presence of cell boundaries. Finally, these methods produce bounding boxes to localize the regions of interest. Bounding boxes are not adequate for delimiting cancerous regions, which may not have regular shapes that can be well captured with boxes. Methods that provide pixel-wise masks are more suitable. For these reasons, we were unable to obtain conclusive results with WSOD methods despite our best efforts, and therefore did not include them in our experiments.

For top-down methods, Grad-CAM and Average pooling are equivalent when the last layer (i.e. classification layer) of a model is linear. Since we use ResNet models in our study, this is always verified, meaning that both methods are equivalent. Therefore, we only report results for the Average pooling when evaluating classification performance. We also initially wanted to evaluate Excitation Backprop (Zhang et al., 2018a) but we were unable to obtain a working code for this method using the PyTorch framework[6].

4 Experimental methodology

In this section, we present an experimental evaluation of several deep weakly supervised methods for classification and localization from the previous section that are relevant in histological image analysis. The aim of our experiments is to assess the ability of the selected methods to accurately classify histological images, and localize cancer regions of interest. The experiments are conducted on four public datasets of histology images which are described in Sec. 4.1. Most of the public datasets were made exclusively for classification or segmentation purposes (Daisuke and Shumpei, 2018). Very few datasets have image-level and pixel-level annotation simultaneously. The only dataset that we found that has both types of annotation is GlaS (Sec. 4.1.3) which is not enough for our evaluation. For this reason, we created a dataset with the required annotations by using

[6] https://pytorch.org

a protocol (Sec. 4.2.3) to sample patches from WSIs of the CAMELYON16 dataset (Sec. 4.1.4). Sec. 4.3 provides a brief description of the training setup of the relevant techniques that we selected in our comparative study.

4.1 DATASETS:

We describe in this section the four public datasets of histology images used in our experiments. A brief description of the datasets is presented in Tab. 2.

Table 2: Brief description of the used datasets in our experiments. (seg.: segmentation.)

Dataset	Medical aspect	Type of image	#Images	Number of classes	Image-level labels	Pixel-level labels
BreakHis	Breast cancer	Patches	7 909	2 classes: benign, malignant.	Yes	No
BACH (Part A)	Breast cancer	Patches	400	4 classes: normal, benign, in Situ, invasive	Yes	No
GlaS	Colon cancer	Patches	165	2 classes: benign, malignant	Yes	Yes (gland seg.)
CAMELYON16	Cancer metastases in Lymph Nodes	WSIs	399	2 classes: normal, metastases	Yes	Yes (tumor seg.)

4.1.1 BREAKHIS DATASET:

BreaKHis is a publicly available[7] dataset for microscopic biopsy images of benign and malignant breast tumor (Spanhol et al., 2016b). The images were collected through a clinical study from January 2014 to December 2014, in which all patients referred to the P&D Laboratory[8] with a clinical indication of breast cancer were invited to participate. The institutional review board approved the study and all patients provided their written consent. All the data were anonymized. Samples were generated from the breast tissue biopsy slides stained with H&E. The samples were collected by surgical open biopsy, prepared for histological study and labeled by pathologists of the P&D Lab. The diagnosis of each case was produced by experienced pathologists and confirmed by complementary exams such as immunohistochemestry analysis.

The original images were acquired in three-channel red-green-blue color space (RGB, 24-bit color depth, 8 bit per channel) with resolution of 752×582 using magnifying factors of $40\times$, $100\times$, $200\times$ and $400\times$. The images were then cropped into size 700×460 and saved in Portable Network Graphics format (PNG) with no compression, nor normalization or color standardization. Fig. 8 shows these four magnification on a single image. The dataset is composed of 7 909 images divided into benign and malignant tumors. Tab. 3 summarizes the dataset distribution in terms of number of images per class, magnification factor and patient. The classes benign and malignant are subdivided into different categories. However, in our experiments, we limit ourselves to the two main classes, i.e. benign against malignant. For more details on the dataset, we refer to (Spanhol et al., 2016b).

4.1.2 BACH CHALLENGE DATASET (PART A) 2018:

The Grand Challenge on BreAst Cancer Histology images (BACH)[9] (Aresta et al., 2018), which is a follow-up of the Bioimaging challenge of 2015[10], was organized in 2018 with the aim of advancing state-of-the-art in automatic classification of histology images. A large annotated dataset of H&E stained breast histology images, composed of both microscopy and WSIs, was specifically compiled and made publicly available for the challenge. The challenge is composed of two parts. Part A is based on the microscopy images and dedicated for image classification task, while Part B is based on WSI and considered for image segmentation task. In our experiments, we consider only Part A since

[7] https://web.inf.ufpr.br/vri/databases/breast-cancer-histopathological-database-breakhis

[8] Pathological Anatomy and Cytopathology, Parana, Brazil: http://www.prevencaoediagnose.com.br

[9] https://iciar2018-challenge.grand-challenge.org/

[10] http://www.bioimaging2015.ineb.up.pt/challenge_overview.html

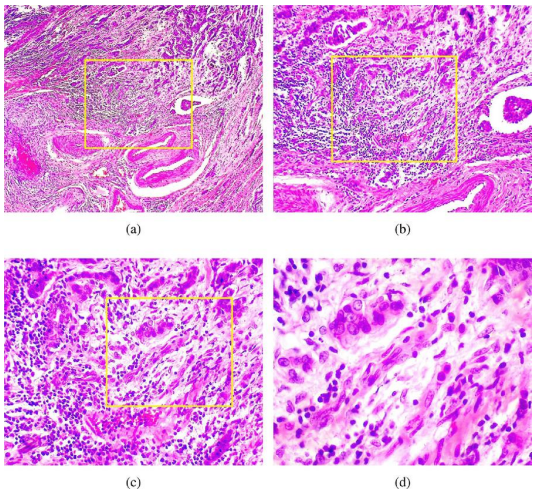

Figure 8: BreakHis dataset: Slides of breast malignant tumor (stained with H&E) seen in different magnification factors: (a) $40\times$, (b) $100\times$, (c) $200\times$, and (d) $400\times$. Highlighted rectangle, which is manually added for illustration purposes only, is the area of interest selected by pathologist to be detailed in the next higher magnification factor (Credit: (Sudharshan et al., 2019)).

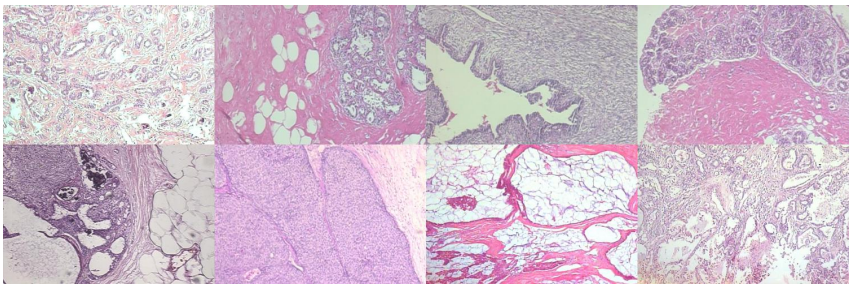

Figure 9: Samples from test set of fold 1 (Spanhol et al., 2016a) from BreaKHis dataset. *Row 1*: Benign. *Row 2*: Malignant.

Table 3: BreakHis dataset (Spanhol et al., 2016b) distribution by class, magnification factor, and patient.

Magnification	Benign	Malignant	Total
$40\times$	625	370	1 995
$100\times$	644	1 437	2 081
$200\times$	623	1 390	2 013
$400\times$	588	1 232	1 820
Total	2 480	5 429	7 909
#Patients	24	58	82

working directly on WSIs adds a heavy complexity to the learning algorithms in terms of memory and running time (Sec. 2.3).

The microscopy dataset is composed of 400 training images and 100 test images distributed evenly between four classes (image level labels): normal, benign, *in situ*, and invasive. Fig. 10 illustrates some examples from different classes. All images were acquired in 2014, 2015, and 2017 using Leica DM 2000 LED microscope and Leica ICC50 HD camera. All patients are from the Covilhã and

Porto regions (Portugal). The annotation was performed by two medical experts. Images where there was disagreement between the normal and benign classes were discarded. The remaining doubtful cases were confirmed via immunohistochemical analysis. The provided images are in RGB Tagged Image File Format (TIFF). All the images have the same size $2\,048 \times 1\,536$ pixels and a pixel scale of $0.42\mu m \times 0.42\mu m$. (Aresta et al., 2018) provide more details on the challenge and the provided data.

In our experiments, we consider a classification task with the four classes of the dataset. The challenge made public images of the train and test sets. However, only train labels are provided. A model prediction must be uploaded to the website of the challenge for evaluation on the test set. Only three trials are allowed per day. Therefore, we limit ourselves to use only the train set for training and evaluation using a cross-validation scheme. We take half of the samples of each class to build the test set and we apply k-fold over the left samples to build the validation and train set.

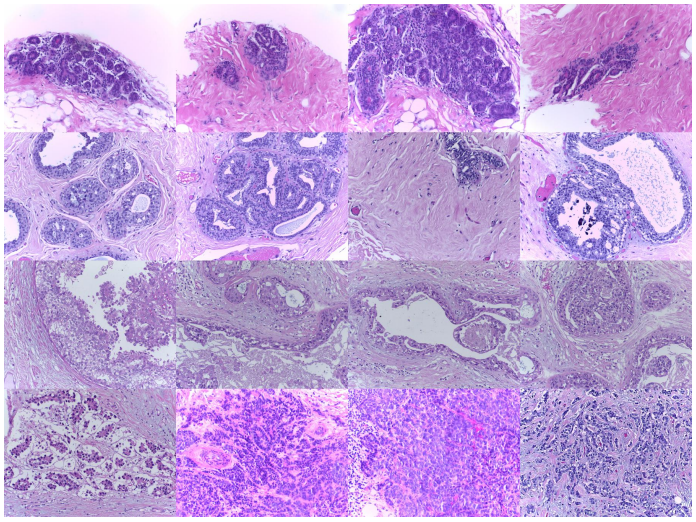

Figure 10: Samples from BACH public train dataset. *Row 1*: Normal. *Row 2*: Benign. *Row 3*: In Situ. *Row 4*: Invasive.

4.1.3 GLAS DATASET:

Colorectal adenocarcinoma originating in intestinal glandular structures is the most common form of colon cancer (Sirinukunwattana et al., 2017). The morphology of intestinal glands, including architectural appearance and glandular formation is used in clinical practice by pathologists to inform prognosis and plan treatment of individual patients. Achieving good inter-observer as well intra-observer reproducibility of cancer grading is a major challenge in the pathology domain. The Gland Segmentation in Colon Histology Images Challenge Contest[11] (Sirinukunwattana et al., 2017) was held in 2015 with the aim to advance automated approaches for quantifying the morphology of glands.

The challenge provides a dataset, GlaS, composed of 165 images derived from 16 H&E histological sections of two grades (classes): benign, and malignant (Fig. 11). The digitization of these histological sections into WSI was accomplished using a Zeiss MIRAX MIDI Slide Scanner with a pixel resolution of $0.465\mu m$. The WSI were subsequently rescaled to a pixel resolution of $0.620\mu m$ (equivalent to $20\times$ objective magnification). Tab. 4 summarizes the partitioning of the dataset with the images size details. (Sirinukunwattana et al., 2017) provide more information on the dataset.

Since the challenge was primarily made for segmentation, a ground truth of the gland segmentation is provided (pixel-level annotation). Aside the segmentation labels, image-level labels are also provided with two classes: benign, or malignant.

[11] https://warwick.ac.uk/fac/sci/dcs/research/tia/glascontest

In this dataset, the glands are the regions of interest that the pathologists use to prognosis the image grading of being benign or malignant. Therefore, in our later experiments (Sec. 5), we are interested in measuring how well the model relies on such medically-valid regions of interest to predict the global class of the image. Therefore, the localized regions by the model are considered as a visual interpretability tool to justify the model's decision. We note that only image-level labels are used during the training, while pixel-level labels are used to evaluate the accuracy of localizing regions of interest (i.e. glands). In our experiments, Test Part A, B are mixed (Tab. 4).

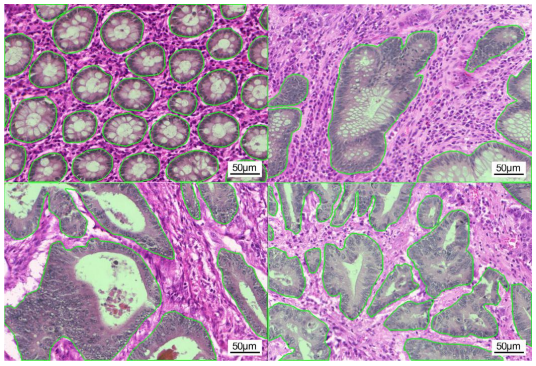

Figure 11: Example of images of different classes with their segmentation from GlaS dataset (Credit: (Sirinukunwattana et al., 2017)). *Row 1*: Benign. *Row 2*: Malignant.

Table 4: Details of the GlaS dataset (Sirinukunwattana et al., 2017).

	Number of Images (Width×Height in Pixels)					
Histologic Grade	Training Part		Test Part A		Test Part B	
Benign	37	1 574 × 433 1 589 × 453 35 775 × 522	33	1 574 × 433 4 589 × 453 28 775 × 522	4	775 × 522
Malignant	48	1 567 × 430 3 589 × 453 44 775 × 522	27	1 578 × 433 2 581 × 442 24 775 × 522	16	775 × 522

4.1.4 CAMELLYON16 DATASET:

The Cancer Metastases in Lymph Nodes Challenge 2016 (CAMELLYON16)[12] competition (Ehteshami Bejnordi et al., 2017) was organized to investigate the potential of machine learning algorithms for detection of metastases in H&E stained tissue sections of sentinel auxiliary lymph nodes (SNLs) of women with breast cancer.

The organizers of the challenge collected 399 WSIs of SNLs during the first half of 2015. SNLs were retrospectively sampled from 399 patients that underwent surgery for breast cancer at 2 hospitals in the Netherlands: Radboud University Medical Center (RUMC) and University Medical Center Utrecht (UMCU). The need for informed consent was waived by the institutional review board of RUMC. The WSIs were acquired at two different centers using two different scanners. RUMC images were produced with a digital slide scanner (Pannoramic 250 Flash II; 3DHISTECH) with a 20× objective lens (specimen-level pixel size, $0.243\mu m \times 0.243\mu m$). UMCU images were produced using a digital slide scanner (NanoZoomer-XR Digital slide scaner C12000-01; Hamamatsu Photonics)

[12] https://camelyon16.grand-challenge.org/Home

with a $40\times$ objective lens (specimen-level pixel size, $0.226\mu m \times 0.226\mu m$). The WSIs are annotated globally to normal or metastases. The WSIs with metastases are further annotated at pixel-level to indicate regions of tumors. The annotations were first drawn by two students (one from each hospital), and then every slide was checked in details by one of the two expert pathologists (one from RUMC and the second from UMCU). In case of uncertainty, pathologist opt to use immunohistochemistry to resolve the diagnostic. An example of a WSI is provided in Fig. 12. Among the provided 399 WSIs, 270 are used for training (111, 159 with and without nodal metastases), and 129 for test (49, 80 with and without nodal metastases)[13]. (Ehteshami Bejnordi et al., 2017) provide more details on the dataset, the challenge, and its final results.

Two tasks were defined in the challenge: identification of individual metastases in WSIs (task 1), and classification of every WSI as either containing or lacking SNL metastases (task 2). The WSIs are extremely large (many gigabytes per image and a resolution of $\sim 100,000^2$ pixels for each image) which makes it inconvenient to conduct our experiments for the purposes of this survey. Therefore, we consider neither of the two tasks. However, we design a concise protocol to assess the different models' capacity in localizing regions of interest at pixel-level (Sec. 4.2). Our protocol consists in building a weakly supervised learning scenario for pixel-wise localization through a binary classification task (normal against metastases) where we have both pixel-level and image-level labels and only image-level labels are used for training. In order to build train, validation, and test sets, we sample a set of patches from the WSIs where a patch is given an image-level label of metastases or normal depending on whether it contains cancerous pixels or not. If it is a metastatic patch, a binary mask that indicates the cancerous pixels is constructed based on the WSI pixel-level annotation.

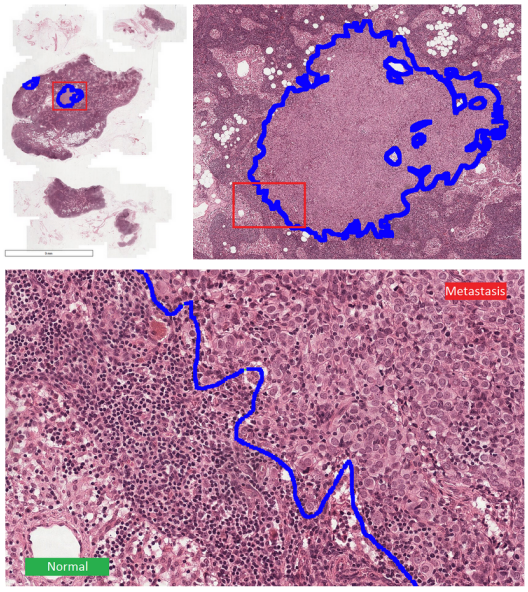

Figure 12: Example of metastatic regions in a WSI from CAMELYON16 dataset (Credit: (Sirinukunwattana et al., 2017)). *Top left*: WSI with tumor. *Top right*: Zoom to one of the metastatic regions. *Bottom*: Further zoom into the frontier between normal and metastatic regions.

4.2 Experimental protocol:

4.2.1 Performance metrics:

In our experiments, we seek to evaluate a model's capacity to accurately classify an image, and locate regions of interest at pixel-level. As described below, we consider two types of evaluation metrics: Evaluation A and Evaluation B.

[13] Sample `test_114` is discarded since the pixel level annotation was not provided. Therefore, the test set is composed of 128 samples with 48 samples with nodal metastases.

Evaluation A. In this evaluation setup we focus only on a model's performance in terms of classification. As evaluation metric, we consider using the accuracy measure:

$$\text{accuracy} = 100 \ \frac{\text{\#correctly classified samples}}{\text{\#samples}} \ (\%) \ , \tag{17}$$

where *#correctly classified samples* is the total number of correctly classified samples, and *#samples* is the total number of samples; and the mean Average Precision measure (Su et al., 2015) (mAP),

$$\text{mAP} = \frac{1}{c} \sum_{k=1}^{c} \text{AP}_k \ 100 \quad (\%) \ , \tag{18}$$

where c is the total number of classes, and AP_k is the average precision of the class k. A perfect model has 100% accuracy and 100% mAP. In this setup, all the relevant models are evaluated on the BreaKHis (Spanhol et al., 2016b) and BACH (Part A) (Aresta et al., 2018) datasets. The image-level labels are the only required supervised annotation for the training and evaluation of the models.

Evaluation B. In this evaluation setup we focus mainly on the performance of a model in terms of pixel-wise localization of regions of interest. To this end, we rely on standard segmentation metrics. In our experiments, we consider Dice index metric (Dice, 1945) which is a measure of agreement or similarity between two sets of samples. Give $\mathbb{G}$ a set of pixels belonging to a ground truth object, and $\mathbb{S}$, a set of pixels belonging to a segmented object. Dice index is defined as follows,

$$\text{Dice}(\mathbb{G}, \mathbb{S}) = \frac{2|\mathbb{G} \cap \mathbb{S}|}{|\mathbb{G}| + |\mathbb{S}|} \ , \tag{19}$$

where $|\cdot|$ denotes set cardinality, $\mathbb{G} \cap \mathbb{S}$ is the set of overlapped pixels between $\mathbb{G}$ and $\mathbb{S}$. Dice index ranges in the interval $[0, 1]$, where the higher the value, the more concordant the segmentation and the ground truth. A Dice index of 1 indicates a perfect segmentation. To compute the Dice index, the pixel-level annotation is required. In the context of evaluating weakly supervised localization models, such annotation is exclusively used for evaluation –i.e. it is not used for training–. Only image-level annotation is used for training. GlaS (Sirinukunwattana et al., 2017), and a variant of CAMELYON16 (Ehteshami Bejnordi et al., 2017) (Sec. 4.2.3) datasets are used for this evaluation. Classification performance at image-level is reported as well.

The aim of this type of evaluation is to measure how well a model, that is trained over a weakly supervised localization task –i.e. using only image-level annotation and deprived from pixel-level annotation–, can localize regions of interest that practically require pixel-level supervision. Such weakly supervised models are compared with an ideal model that is trained for segmentation only using pixel-level annotation without image-level annotation –i.e. segmentation task–. In this context, we consider using the model U-Net (Ronneberger et al., 2015) which is a reference model in medical image segmentation. Such a model is trained exclusively on pixel-level annotation: In the case of GlaS we train the model to segment the glands; while in the case of CAMELYON16 we train it to segment cancerous regions.

We note that in the case of the GlaS dataset (Sec. 4.1.3), and the case of weakly supervised model that outputs two features maps to indicate regions of interest, Dice index is computed using the heat map corresponding to the true image-level label. In the case of CAMELYON16 dataset (Sec. 4.1.4), Dice index is computed with respect to the heat map that corresponds to the metastatic class. This implies that we perform the evaluation only on the samples with metastatic image-level label. We also compute average Dice index over both metastatic and normal classes.

4.2.2 Datasets organization:

In our experiments, the test set is fixed in all the datasets, and only train and validation sets are changed using a k-fold scheme. The only exception to the fixed test set rule is BreakHis where we use the provided folding (Spanhol et al., 2016a) where each fold, and each magnification has its own test set. However, we apply the k-fold over the provided train set to obtain the train and validation sets. In our experiments, given the provided train set, we take 20% of the samples for validation, and 80% for actual training. This leads to 5-folds partitioning. We report the average of the mean and the standard deviation of each metric over the trials in the following form: mean $\pm$ standard deviation.

We note that BreaKHis and BACH (Part A) datasets are used for **Evaluation A** (Sec. 4.2.1) while GlaS and CAMELYON16 are used for **Evaluation B** (Sec. 4.2.1). The results of our experiments on BreaKHis, BACH (Part A), GlaS, and CAMELYON16 are presented in Tables 6, 7, 8, 9 and 10. We note that in order to compute Dice index for a set, we average Dice index of each image, unless stated otherwise.

The deterministic code used to create the folds of all the datasets, sampling from CAMELYON16, the coordinates of the sampled patches from CAMELYON16, and the code of all the experiments is publicly available[14].

4.2.3 CAMELYON16 PROTOCOL FOR WEAKLY SUPERVISED LOCALIZATION:

We describe in this section our protocol of creating a weakly supervised localization dataset from CAMELYON16 dataset (Ehteshami Bejnordi et al., 2017). Samples are patches from WSIs, and each patch has two levels of annotation:

- Image-level label y: the class of the patch, where $y \in \{\texttt{normal}, \texttt{metastatic}\}$.
- Pixel-level label $\boldsymbol{Y} = \{0,1\}^{H^{\text{in}} \times W^{\text{in}}}$: a binary mask where the value 1 indicates a `metastatic` pixel, and 0 a `normal` pixel. For `normal` patches, this mask will contain 0 only.

First, we split CAMELYON16 dataset into train, validation, and test set at *WSI-level* as described in Sec. 4.2.1. This prevent patches from the same WSI to end up in different sets. All patches are sampled with the highest resolution from WSI –i.e. level $= 0$ in WSI terminology–. We present in the following our methodology of sampling metastatic and normal patches.

Sampling metastatic patches. Metastatic patches are sampled only from metastatic WSIs around the cancerous regions. Sampled patches will have image-level label, and a pixel-level label. The sampling follows these steps: 1. Consider a metastatic WSI. 2. Sample a patch $\mathbf{x}$ with size (H, W). 3. Binarize the patch into $\boldsymbol{x}^{\text{b}}$ mask using OTSU method (Otsu, 1979). Pixels with value 1 indicate tissue. 4. Let $p_t^{\boldsymbol{x}^{\text{b}}}$ be the tissue percentage within $\boldsymbol{x}^{\text{b}}$. If $p_t^{\boldsymbol{x}^{\text{b}}} < p_t$, discard the patch. 5. Compute the metastatic binary mask $\boldsymbol{Y}$ of the patch $\mathbf{x}$ using the pixel-level annotation of the WSI (values of 1 indicate a metastatic pixel). 6. Compute the percentage $p_m^{\boldsymbol{x}}$ of metastatic pixels within $\boldsymbol{Y}$. 7. If $p_m^{\mathbf{x}} < p_0$, discard the patch. Else, keep the patch $\mathbf{x}$ and set $y = \texttt{metastatic}$ and $\boldsymbol{Y}$ is its pixel-level annotation.

We note that we sample *all* possible metastatic patches from CAMELYON16 using the above approach. Sampling using such approach will lead to a large number of metastatic patches with high percentage of cancerous pixels (patches sampled from the center of the cancerous regions). These patches will have their binary annotation mask $\boldsymbol{Y}$ full of 1. Using these patches will shadow the performance measure of localization of cancerous regions. To avoid this issue, we propose to perform a calibration of the sampled patches in order to get rid of most of such patches. We define two categories of metastatic patches: 1. **Category 1**: Contains patches with $p_0 \leq p_m^{\mathbf{x}} \leq p_1$. Such patches are rare, and contain only small region of cancerous pixels. They are often located at the edge of the cancerous regions within a WSI. 2. **Category 2**: Contains patches with $p_m^{\mathbf{x}} > p_1$. Such patches are extremely abundant, and contain a very large region of cancerous pixels (most of the time the entire patch is cancerous). Such patches are often located inside the cancerous regions within a WSI.

Our calibration method consists in keeping all patches within **Category 1**, ans discarding most of the patches in **Category 2**. To this end, we apply the following sampling approach: 1. Assume we have n patches in **Category 1**. We will sample $n\ p_n$ patches from **Category 2**, where p_n is a predefined percentage. 2. Compute the histogram of the frequency of the percentage of cancerous pixels within all patches. Assuming a histogram with b bins. 3. Among all the bins with $p_m^{\mathbf{x}} > p_1$, pick uniformly a bin. 4. Pick uniformly a patch within that bin.

This procedure is repeated until we sample $n\ p_n$ patches from **Category 2**. Tab. 5 presents the number of sampled patches from the entire CAMELYON16 dataset, before and after calibration. We note that the sampling of metastatic patches is done separately on the original provided train, and test sets of WSIs.

[14] https://github.com/jeromerony/survey_wsl_histology

In our experiments, patches are not overlapping. We use the following configuration: $p_0 = 20\%$, $p_1 = 50\%$, $p_t = 10\%$, $p_n = 1\%$. The number of bins in the histogram is obtained by dividing the interval $[0, 1]$ with a delta of 0.05. We investigate the following patch sizes: 512×512, 768×768 and $1\,024 \times 1\,024$. In one experiment, only one patch size is used –i.e. patches with different sizes are not mixed within the same set–. Fig. 13 illustrates an example of metastatic patches and their corresponding masks.

We note that metastatic patches are sampled then calibrated only once from the original train, and test WSI. Therefore, each WSI has a *unique* and *unchanged* set of metastatic patches.

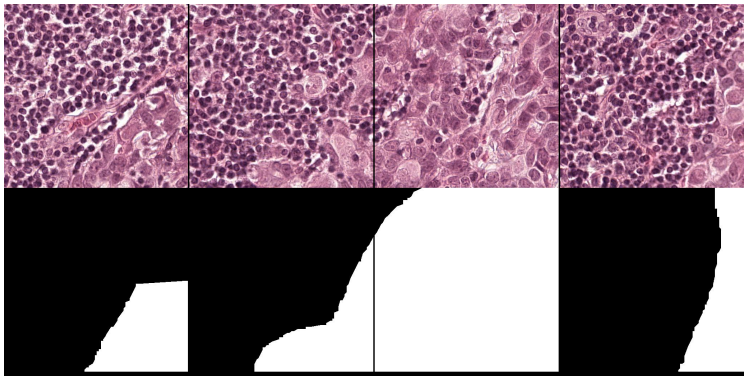

Figure 13: Example of metastatic patches with size 512×512 sampled from CAMELYON16 dataset (WSI: `tumor_001.tif`). *Top row*: Patches. *Bottom row*: Masks of metastatic regions (white color).

Table 5: Total number of metastatic patches sampled from the entire CAMELYON16 dataset (Ehteshami Bejnordi et al., 2017) using our sampling approach; and diffrent patch sizes. Patches are not overlapping.

	#Patches: Before calibration			#Patches: After calibration	
Patch size	Total	$p_0 \leq p_m^{\mathbf{x}} \leq p_1$	$p_m^{\mathbf{x}} > p_1$	Total	$p_m^{\mathbf{x}} > p_1$
512×512	137 769	14 912	122 857	24 435	9 523
768×768	64 127	9 512	54 615	15 377	5 865
$1\,024 \times 1\,024$	37 598	6 988	30 610	11 470	4 482

Sampling normal patches. Normal patches are sampled only from normal WSI. A normal patch is sampled randomly and uniformly from the WSI (without repetition nor overlapping). If the patch has enough tissue ($p_t^{\mathbf{x}^{\mathrm{b}}} \geq p_t$), the patch is accepted. The measure of tissue mass is performed at level $= 6$ where it is easy for the OTSU binarization method to split the tissue from the background. We double-check the tissue mass at level $= 0$.

Let us consider a set (train, validation, or test) at patch level within a specific fold. We first pick the corresponding metastatic patches from the metastatic WSI, assuming n_m is their total number. Assuming there is h normal WSIs in this set, we sample the same number of normal patches as the total number of metastatic ones. In order to mix the patches from all the normal WSI, we sample $\frac{n_m}{h}$ normal patches per normal WSI. In our experiment, we use the same setup as in the case of sampling metastatic patches: $p_t = 10\%$. Fig. 14 illustrates an example of normal patches. This sampling procedure implies that metastatic patches are fixed in all the metastatic WSI (also, they are the same across folds), while normal patches within a normal WSI change across folds.

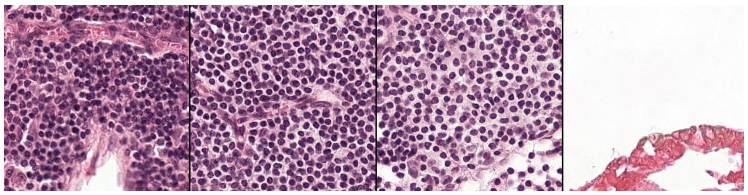

Figure 14: Example of normal patches with size 512×512 sampled from CAMELYON16 dataset (WSI: `normal_001.tif`).

4.3 Training setup:

4.3.1 Weakly supervised training:

For all the methods, we employed the ResNet-18 architecture (He et al., 2016) pre-trained on the ImageNet dataset and used the cross-entropy loss during training. Following transfer learning methods, we remove the last dense layers, and preserve the pre-trained convolutional layers as feature extractors. This allows to reduce over-fitting due to the limited number of training samples. The per-class scores are obtained using one of the studied spatial pooling methods (average, max, LSE, or WILDCAT pooling). Therefore, the models are fully convolutional, which helps for spatial localization. With the Deep MIL model, we duplicated the scoring and pooling layers to match the number of classes, while using ResNet18 as a feature extractor. The optimization algorithm used is Stochastic Gradient Descent (SGD) with Nesterov acceleration, using a momentum of 0.9 and weight decay of 0.0001. The learning rate is set to 0.01 for the first half of the training, and decayed to 0.001 for the second half. These learning hyper-parameters were chosen empirically, based on the convergence of loss functions on validation data. The mini-batch size is set to 64 for all datasets except GlaS where it is set to 32 because of the rather small size of the dataset. For all datasets, we randomly flip the images during training. We also perform random color jittering on the images with parameters $\mathrm{brightness}$, $\mathrm{contrast}$ and $\mathrm{saturation}$ at 0.5 and hue at 0.05 (from the PyTorch framework). The classification loss over the validation set is used for model selection over training epochs (early stopping).

To train models using mini-batches, we must scale images to a common size. Since these images have different sizes between and within datasets, cropping and resizing strategies differ between datasets. In all our experiments, a cropped patch extracted from an image inherits the same global label of its image.

For BACH dataset, the image size is large $2\,048 \times 1\,536$. Therefore, we train on patches extracted from the images; and each patch receives the image label. The extracted patches have a size of 512×512 at random locations and random rotations while ensuring that no empty zone is included (which happens when sampling too close to the borders of the image depending on the angle of rotation). We train all the models during 20 epochs. For the BreakHis and GlaS datasets, we extract patches of size 448×448 and 416×416 respectively at random locations and rotate them with a random angle in $\{0°, 90°, 180°, 270°\}$. For the BreakHis dataset, the models are trained during 80 epochs and for GlaS dataset, they are trained for 160 epochs since the number of samples is very small. For CAMELYON16 dataset, the images are simply rotated with a random angle in $\{0°, 90°, 180°, 270°\}$. The models are trained for 20 epochs.

For LSE and WILDCAT pooling, choosing the optimal hyper-parameters is challenging since we seek to obtain the highest level of performance in both classification and localization (segmentation) tasks. Since the models are classification-based, we studied the effect of pooling hyper-parameter on the classification loss using a validation set, and examined the segmentation performances on the test set for LSE and WILDCAT on GlaS with these hyper-parameters. For LSE, we considered values of $q \in \{0.03, 0.1, 0.3, 1, 3, 10\}$ and for WILDCAT, we limited the search to $n^+ = n^-$ with values of $\alpha \in \{0, 0.2, 0.4, 0.6, 0.8, 1\}$ and $n^+ \in \{0.05, 0.1, 0.2, 0.3, 0.4, 0.5\}$ ($n^+ = n^- = 0.5$ corresponds to using the entire activation maps for the final score). We observed that the variations in results are small. For LSE, the minimum validation losses are all within standard deviation of each other,

suggesting that adjusting q does not significantly impact the classification performance. We also observed that the impact on the dice index is also rather small. For WILDCAT, the differences are larger in term of validation loss, although the differences in final performance for classification and segmentation are much smaller. Overall, the segmentation performances seem robust to variations of the pooling hyper-parameters, when these are validated over the classification loss. We also ran single-fold experiments with LSE on Camelyon, and observed a similar trend. These validation experiments motivated our choice for following the hyper-parameters in Sun et al. (2016) for LSE ($q = 10$) and in Durand et al. (2017) for WILDCAT. For the LSE pooling, we set $q = 10$ as in Sun et al. (2016). For WILDCAT, we set $n^+ = n^- = 10\%$ and $\alpha = 0.6$ as one of the many studied values in Durand et al. (2017).

For BreakHis and BACH datasets, we also study the impact of the number of training samples by training with only a fraction of each dataset. For both datasets, we do not change the size of the validation set nor the test set. To reduce the size of the training set, we randomly sample a given fraction of the examples in each class to keep the same balance between the classes. For BACH, we use the following percentages: $10\%, 25\%, 50\%, 75\%, 100\%$ which corresponds to the following number of training samples *per class*: $4, 10, 20, 30, 40$, respectively. For BreakHis, we use the following percentages: $4\%, 10\%, 25\%, 50\%, 75\%, 100\%$. Since each magnification has a different number of samples, and for clarity, we prefer to not mention the per class number of samples. However, they can be easily computed based on Tab. 3.

Challenges in model selection and hyper-parameters tuning for WSL: While this goes beyond the scope of this survey, model selection and hyper-parameter tuning is an important issue with WSL models that is, unfortunately, overlooked in the literature. Large explorations of the hyper-parameter space may potentially help the supervised task (in our case, the classification task) since the model selection relies on a supervised classification error over a validation set. However, the hyper-parameters obtained using such a search are not guaranteed to be the best for the unsupervised task (in our case, the pixel-level localization task). This may lead to an inefficient search for hyper-parameters that favors the supervised task, independently of the domain and the explored grid. For example, with all the dataset in the experiments, the classification accuracy for all the models seems to stagnate at a maximum value, and searching beyond these hyper-parameters is unjustified.

4.3.2 Fully supervised training:

We also train a fully supervised U-Net architecture (Ronneberger et al., 2015) on GlaS and CAMELYON16 datasets to obtain an upper bound performance in terms of pixel-wise localization in a fully supervised setting. For both datasets, we train the model to minimize a standard pixel-wise cross-entropy using SGD with Nesterov acceleration with a momentum of 0.9 and a weight decay of 0.0001. The learning rate is set to 0.1 and decayed during training depending on the number of epochs to reach 0.001 at the end of the training. For both datasets, the mini-batch size is set to 16. The supervised segmentation loss obtained on the validation set was used for model selection over training epochs.

For the GlaS dataset, models are trained for 960 epochs and the learning rate is divided by 10 at every 320 epochs. For the CAMELYON16 dataset, models are trained for 90 epochs and the learning rate is divided by 10 every 30 epochs. We use the same augmentations as in the weakly-supervised training for both datasets (Sec. 4.3.1).

5 Results, interpretation, and future directions

5.1 Evaluation A – classification performance:

Tables 6, 7, 8 and 9 display the performance for the different deep WSL models on the four datasets in terms of classification accuracy, and average precision (AP) or mean average precision (mAP) in the case of a multi-class dataset. For this evaluation, the performance of Grad-CAM is not reported since the method is identical to CAM for classification. Results indicate that these models achieved similar high classification performance on GlaS (Tab. 8) and CAMELYON16 (Tab. 9) datasets ($\sim 100\%$)

Table 6: **Evaluation A**: Accuracy and AP of deep WSL models over test folds of the BreakHis dataset using different magnification factors.

Method \ Magnification	40×		100×		200×		400×	
	Accuracy (%)	**AP (%)**	**Accuracy (%)**	**AP (%)**	**Accuracy (%)**	**AP (%)**	**Accuracy (%)**	**AP (%)**
CAM - Average	92.19 ± 3.54	97.80 ± 2.30	89.64 ± 2.93	98.10 ± 0.91	91.03 ± 1.33	98.36 ± 0.54	85.09 ± 2.09	96.04 ± 0.99
Max	90.09 ± 2.89	97.64 ± 2.01	88.11 ± 3.08	97.75 ± 1.22	90.41 ± 2.66	98.21 ± 0.70	84.00 ± 1.95	95.44 ± 1.16
LSE	89.52 ± 3.68	97.04 ± 2.96	89.57 ± 3.24	97.92 ± 1.00	90.15 ± 1.96	98.08 ± 0.79	84.86 ± 1.98	95.16 ± 1.74
WILDCAT	92.40 ± 2.82	97.90 ± 2.41	90.22 ± 2.48	97.99 ± 1.55	90.75 ± 2.00	98.49 ± 0.59	85.85 ± 3.05	96.41 ± 1.40
Deep MIL	91.80 ± 2.70	98.38 ± 1.64	89.54 ± 3.14	97.69 ± 1.16	91.61 ± 1.34	98.71 ± 0.55	85.98 ± 2.28	96.29 ± 0.85

Table 7: **Evaluation A**: Accuracy and mAP of deep WSL models over test folds of the BACH (Part A) dataset.

Method	**Accuracy (%)**	**mAP (%)**
CAM - Average	84.10 ± 2.51	93.23 ± 1.27
Max	76.10 ± 3.60	87.34 ± 4.44
LSE	78.90 ± 4.29	88.73 ± 2.77
WILDCAT	84.80 ± 1.25	93.04 ± 1.00
Deep MIL (adapted)	83.30 ± 3.90	92.68 ± 2.71

Table 8: **Evaluation A and B**: Dice index, accuracy of deep WSL models over the test folds of the GlaS dataset. AP is not shown since weakly supervised localization methods always achieve 100%.

Method	**Dice index**	**Accuracy (%)**
CAM - Average	68.43 ± 0.73	99.75 ± 0.56
GradCAM	68.48 ± 0.72	99.75 ± 0.56
Max	67.51 ± 2.48	99.75 ± 0.56
LSE	67.45 ± 1.54	99.75 ± 0.50
WILDCAT	68.62 ± 0.61	100 ± 0
Deep MIL (adapted)	72.13 ± 1.78	99.25 ± 1.12
U-Net	90.54 ± 0.88	-

Table 9: **Evaluation A**: Accuracy and AP obtained with weakly supervised localization models for test folds of CAMELYON16 (Ehteshami Bejnordi et al., 2017) dataset using increasing patch size.

Method \ Patch size	512×512		768×768		$1\,024 \times 1\,024$	
	Accuracy (%)	**AP (%)**	**Accuracy (%)**	**AP (%)**	**Accuracy (%)**	**AP (%)**
CAM - Average	98.54 ± 0.36	99.80 ± 0.04	98.37 ± 0.45	99.89 ± 0.03	99.20 ± 0.28	99.92 ± 0.02
Max	98.51 ± 0.22	99.80 ± 0.04	98.62 ± 0.27	99.90 ± 0.04	99.23 ± 0.36	99.94 ± 0.01
LSE	98.62 ± 0.22	99.80 ± 0.04	98.77 ± 0.22	99.92 ± 0.02	98.88 ± 0.47	98.93 ± 0.05
WILDCAT	98.37 ± 0.65	99.84 ± 0.05	98.62 ± 0.36	99.92 ± 0.03	99.16 ± 0.17	99.95 ± 0.01
Deep MIL	98.15 ± 0.59	99.82 ± 0.04	98.34 ± 1.16	99.82 ± 0.23	99.17 ± 0.11	99.95 ± 0.01

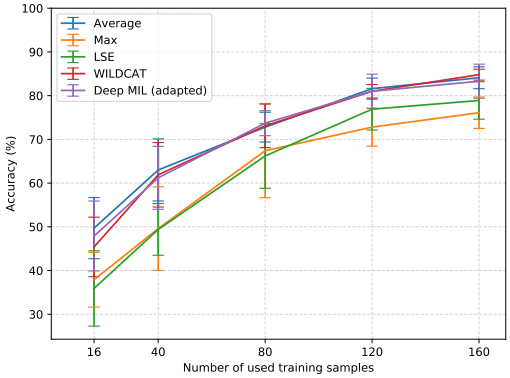

Figure 15: Influence of the training set size for the BACH dataset.

with low variation. This suggests that both datasets are not challenging for a classification task. For BreakHis (Tab. 6) and BACH (Tab. 7), we observe that the classification performance is high and similar for CAM, WILDCAT and Deep MIL (even adapted to the multi-class scenario), but and lower for LSE and Max with generally high standard deviations. This confirms the observation made by Zhou et al. (2016) that LSE and Max pooling strategies tend to overfit, especially when training on few samples.

Tab. 6 shows that the classification performance of studied models on BreakHis data (both in terms of accuracy and AP) is generally at its highest level with $200\times$ and $40\times$ magnifications. This is further confirmed by the accuracy obtained when training only on a fraction of the dataset Fig. 16. When using 25% of the training set, the accuracy of most models is still around $\sim 90\%$ at magnification of $200\times$ and $40\times$ as opposed to $100\times$ and $400\times$ magnification. However, the magnification $200\times$ seems to be more stable and robust to variation of the number of training samples. The magnification $400\times$ is shown to provide the lowest performance. To obtain discriminative features for cancer grading, results indicate that these models should observe images at a lower magnification (zoomed out) – i.e. between $40\times$ and $200\times$. Zooming into the histology image – e.g. $400\times$ – makes it difficult to discriminate between the different classes. This may also suggest that when zooming in further, this type of imaging provides almost similar images independently of the cancer grade.

Fig. 16 shows that the classification accuracy of Deep MIL varies considerably with the BreakHis dataset when the number of training samples is reduced, which suggests that this method needs a larger number of training sample to achieve a higher level of accuracy. In the case of BACH dataset, increasing the size of the training samples leads to an improvement in classification performance across all the methods (Fig. 15) which is a typical behavior in ML algorithms. Figures 15 and 16 also suggest that in order to obtain a high level of classification accuracy of $\sim 80\%$, models require at least ~ 40 samples per class for BACH dataset, and ~ 40 samples per class for BreakHis ($\sim 10\%$).

5.2 Evaluation B – pixel-wise localization performance:

Tables 8 and 10 correspond to the evaluation of different deep weakly supervised localization techniques over GlaS and CAMELYON16 datasets, respectively, in terms of localization performance. In terms of Dice index, we observe that Deep MIL obtains the best performance on GlaS dataset while Max and LSE pooling have worse results and higher variation. This suggests that both methods have a tendency to overfit more and they are more sensitive to data variations through cross-validation. For the CAMELYON16 dataset, we notice that all the methods except Deep MIL achieve relatively similar Dice index over the entire test set. Max and LSE have much lower performance on large patches. This is due to the fact that these methods tend to overfit on small discriminative regions which represent a much smaller fraction of the images in a large patch which results in a low Dice index. The performance in terms of Dice index of Deep MIL is however not representative due the way we have adapted it. It tends to predict positive –i.e. metastatic– regions all over the images.

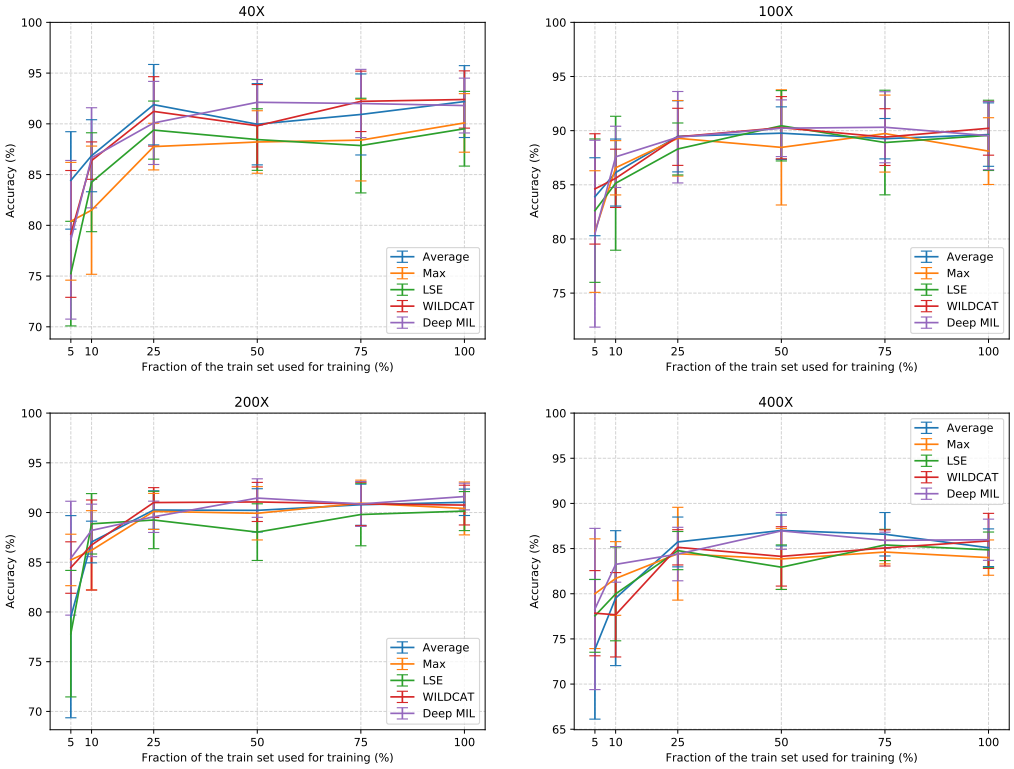

Figure 16: Influence of the training set size for the BreakHis dataset at magnification levels of $40\times$ (top left), $100\times$ (top right), $200\times$ (bottom left) and $400\times$ (bottom right).

Table 10: **Evaluation B**: Dice index over all pixels and averaged over all metastatic images (mDice metastatic) obtained with weakly supervised localization models for test folds of CAMELYON16 (Ehteshami Bejnordi et al., 2017) dataset using a increasing patch size.

Patch size / Method	512×512		768×768		$1\,024 \times 1\,024$	
	Dice index	**mDice metastatic**	**Dice index**	**mDice metastatic**	**Dice index**	**mDice metastatic**
CAM - Average	65.06 ± 1.00	62.47 ± 1.17	64.16 ± 0.78	61.45 ± 0.67	66.70 ± 2.77	63.98 ± 2.93
GradCAM	65.18 ± 1.02	62.51 ± 1.19	64.14 ± 0.86	61.35 ± 0.75	66.75 ± 2.76	63.98 ± 2.95
Max	67.08 ± 1.33	62.31 ± 1.10	68.50 ± 1.43	63.51 ± 1.02	62.64 ± 9.18	63.95 ± 1.97
LSE	67.04 ± 1.30	62.78 ± 0.87	64.96 ± 3.96	61.71 ± 1.81	66.67 ± 6.98	63.68 ± 3.48
WILDCAT	66.06 ± 0.84	62.87 ± 0.86	67.24 ± 1.29	63.74 ± 1.33	66.05 ± 2.96	65.52 ± 1.28
Deep MIL	49.26 ± 2.81	69.76 ± 0.73	47.93 ± 2.66	68.49 ± 2.16	46.61 ± 2.81	65.97 ± 1.67
U-Net	77.68 ± 1.47	70.90 ± 2.37	79.90 ± 1.30	73.03 ± 2.05	80.72 ± 0.83	72.79 ± 1.47

For this reason, we also report the mean Dice index over metastatic images to measure how well it predicts positive regions. This measure shows that Deep MIL is able to correctly identify positive regions compared to other techniques.

In Appendix A, we provide visual examples of the predicted masks for pixel-wise localization produced by the different studied deep weakly supervised localization techniques over GlaS and CAMELYON16 test sets of the first split. From Figures 17, 18, 19 and 20, the main observation is the high false positive rate. The models are unable to correctly spot the right regions of interest, and, they tend to be active all over the image.

The deep WSL models have been developed, validated, and improved over the years mainly over natural scene images which reinforce many implicit priors of such type of images in their conception. We believe that applying them directly to histological images for weakly supervised localization tasks can lead to poor and unexpected results in terms of localization of regions of interest as illustrated visually in Figures 17, 18, 19 and 20. This behavior is mainly a direct result of the nature of histological images where regions of interest are highly unstructured, variable in size, multi-instance presence, and more importantly, non-salient. Often, in a histological image, regions of interest have similar visual appearance in terms of texture/color with respect to the background. This may potentially mislead the models and result in a high false positive rate. Therefore, applying the studied weakly supervised localization techniques in histology may require an adaptation to improve the selectivity of regions of interest and reduce false positive rate. A promising approach has been proposed recently where modeling irrelevant regions within the image is taken in consideration which allows to reduce false positives with a large gap (Belharbi et al., 2019). High false positive rates damage the interpretability aspect of weakly supervised localization techniques, and lower their usefulness in a weak localization task in histological images.

Another explanation to the high false positive rate is related to the pooling function. All the models are required to perform a spatial pooling to be able to classify the input image. A model is trained to predict either benign or malignant cancer grade by maximizing the probability of the target class. For a method such as CAM with Average pooling, this will attempt to maximize the probability of the target class by maximizing scores over every location in the image in order to maximize the global probability for that class since all locations in histological images are practically similar in terms of visual perception. Adding to this the issue of noisy labels of patches during training discussed in Sec. 2.3. As a result, this allows to consider non-discirminative regions as discriminative –i.e. consider noise/background as regions of interest–. Therefore, high false positive rate is increased. This problem may be addressed by adding more supervision in the form of size constraints (Jia et al., 2017) for instance. However, this will face the challenge of the high variation of the size of object of interest in histological images that goes from tiny regions to almost cover an entire image. Adding noise –i.e. uncertainty– to the target label at patch level may help reducing the issue of the inconsistency that may raise when transferring the image label to the patch label (Szegedy et al., 2016).

In our evaluation, we only considered the fully-supervised U-Net model as an upper bound. It might be interesting to evaluate more recent state-of-the-art segmentation architectures such as DeepLabV3+ (Chen et al., 2018) and HRNet (Sun et al., 2019) to get a stronger baseline, as these architectures combine the benefits of both ResNet-like architectures (which perform well in classification) and segmentation-specific architectural improvements.

5.3 Future directions:

Based on our results, the application of stat-of-the-art deep WSL models on histological images showed that these techniques can achieve a high level classification accuracy. However, for pixel-wise localization of regions of interest, these models lack accuracy, leading to a high false positive rate for localization, and potentially limiting the interpretability of a model's predictions. This is mainly due to the complex nature of histological images.

While the localization accuracy obtained with full pixel-level supervision incurs a higher annotation cost, our results suggest that training these WSL models without pixel-level labels can result in poor

localization in histological images. As a potential compromise, active and semi-supervised learning, where only few selected training images are labeled at pixel-level, can be a promising research direction for histological image analysis. In both settings, a pathologist would be called upon to annotate some informative images at pixel-level. Given some limited interactions with a pathologist, active learning methods (Settles, 2009) will allow to selectively increase the number of annotated samples during the training phases. Such pixel-level supervision should provide a strong indication about the nature of images regions of interest to be located, which in turn can potentially reduce the false positive rate of localization.

Finally, it is worth noting the challenges related to cancer grading, and its impact on image labels and regions localization. As mentioned in the key challenges of histological images, many grades may be present in the image, yet only the worst grade is provided as image label. Therefore, in order to improve region localization and reduce false positives, the learning process may also leverage the presence of multiple grades by exploiting multi-label learning scenario (instead of considering one single label in the image). This will improve DL model awareness, and prevent it from associating the entire image into one single label.

6 Conclusion

Training deep learning models for cancer grading and localization in histological images normally requires both image- and pixel-level labels. Given the high resolution of histological images, pixel-level labels require a costly and time consuming annotation process. Motivated by this issue, we explore the application of several state-of-the-art deep WSL models –initially proposed in the computer vision community (for natural images)– in histological image analysis, *without* pixel-level annotation.

This paper provides a survey on deep WSL models that are suitable for classification of histological images, and pixel-wise localization of regions of interest that correspond to class predictions. First we describe the process of histological image production, and outline the key challenges for their analysis. Then, we describe a taxonomy of suitable deep WSL techniques in the literature composed of bottom-up and top-down methods, where the former represents the more active in the research community. These methods are analysed with histological image analysis in mind. Promising methods are evaluated and compared experimentally in terms of accuracy (classification and pixel-wise localization) on four different public histological image datasets for breast and colon cancer – BreakHis, BACH, GlaS, and CAMELYON16. In order to provide more histology image benchmarks for large scale evaluation, we propose a concise protocol to build WSL datasets from Whole Slide Images (WSI). This protocol is used to create a new weakly supervised localization benchmark from the CAMELYON16 dataset. The results of our experimental study [15] show that the deep WSL models can provide a very high level of classification accuracy, but also suffer from a high false positive rate for pixel-wise localization. The latter suggests that specialized deep WSL models (e.g., (Belharbi et al., 2019)) are required for pixel-wise localization in such large heterogeneous images, with highly non-salient and unstructured regions. Future research directions include improving performance by leveraging few relevant pixel-level annotations, through semi-supervised and active learning.

References

Aresta, G., Araújo, T., Kwok, S., et al. (2018). Bach: Grand challenge on breast cancer histology images. *coRR*, abs/1808.04277.

Bahdanau, D., Cho, K., and Bengio, Y. (2015). Neural machine translation by jointly learning to align and translate. In Bengio, Y. and LeCun, Y., editors, *ICLR*.

Bamford, P. and Lovell, B. (2001). Method for accurate unsupervised cell nucleus segmentation. In *Conf. of the Intern. Conf. of the IEEE Engineering in Medicine and Biology Society*.

Bankman, I. (2008). *Handbook of medical image processing and analysis*. Elsevier.

[15] Public code: https://github.com/jeromerony/survey_wsl_histology

Bartels, P., Thompson, D., Bibbo, M., et al. (1992). Bayesian belief networks in quantitative histopathology. *Analytical and quantitative cytology and histology*, 14.

Basavanhally, A., Agner, S., Alexe, G., et al. (2008). Manifold learning with graph-based features for identifying extent of lymphocytic infiltration from high grade, her2+ breast cancer histology.

Belharbi, S., Rony, J., Dolz, J., Ben Ayed, I., McCaffrey, L., and Granger, E. (2019). Weakly supervised object localization using min-max entropy: an interpretable framework. *coRR*, abs/1907.12934.

Bency, A. J., Kwon, H., Lee, H., et al. (2016). Weakly supervised localization using deep feature maps. In *ECCV*.

Bilen, H., Pedersoli, M., and Tuytelaars, T. (2014). Weakly supervised object detection with posterior regularization. In *BMVC*.

Bilen, H., Pedersoli, M., and Tuytelaars, T. (2015). Weakly supervised object detection with convex clustering. In *CVPR*.

Bilen, H. and Vedaldi, A. (2016). Weakly supervised deep detection networks. In *CVPR*.

Bilgin, C., Demir, C., Nagi, C., et al. (2007). Cell-graph mining for breast tissue modeling and classification. In *Intern. Conf. of the IEEE Engineering in Medicine and Biology Society*.

Boyd, S. and Vandenberghe, L. (2004). *Convex Optimization*. Cambridge University Press.

Bándi, P., Geessink, O., Manson, Q., et al. (2019). From detection of individual metastases to classification of lymph node status at the patient level: The camelyon17 challenge. *IEEE Transactions on Medical Imaging*, 38.

Caicedo, J. C., González, F. A., and Romero, E. (2011). Content-based histopathology image retrieval using a kernel-based semantic annotation framework. *Jour. of biomedical informatics*, 44.

Caie, P. D., Turnbull, A. K., Farrington, S. M., et al. (2014). Quantification of tumour budding, lymphatic vessel density and invasion through image analysis in colorectal cancer. *Journal of translational medicine*, 12.

Cao, C., Liu, X., Yang, Y., et al. (2015). Look and think twice: Capturing top-down visual attention with feedback convolutional neural networks. In *ICCV*.

Carbonneau, M.-A., Cheplygina, V., Granger, E., and Gagnon, G. (2018). Multiple instance learning: A survey of problem characteristics and applications. *Pattern Recognition*, 77:329–353.

Chandler, D. E. and Roberson, R. W. (2009). *Bioimaging: current concepts in light and electron microscopy*. Jones & Bartlett Publishers.

Chattopadhyay, A., Sarkar, A., Howlader, P., et al. (2018). Grad-cam++: Generalized gradient-based visual explanations for deep convolutional networks. In *WACV*.

Chen, H., Qi, X., Yu, L., et al. (2016). Dcan: deep contour-aware networks for accurate gland segmentation. In *CVPR*.

Chen, L.-C., Zhu, Y., Papandreou, G., Schroff, F., and Adam, H. (2018). Encoder-decoder with atrous separable convolution for semantic image segmentation. In *ECCV*.

Cheplygina, V., de Bruijne, M., and Pluim, J. (2019). Not-so-supervised: A survey of semi-supervised, multi-instance, and transfer learning in medical image analysis. *MIA*, 54.

Cinbis, R. G., Verbeek, J., and Schmid, C. (2017). Weakly supervised object localization with multi-fold multiple instance learning. *IEEE trans. on pattern analysis and machine intelligence*, 39.

Ciompi, F., Geessink, O., Bejnordi, B. E., et al. (2017). The importance of stain normalization in colorectal tissue classification with convolutional networks. In *Biomedical Imaging*.

Cireşan, D. C., Giusti, A., Gambardella, L. M., et al. (2013). Mitosis detection in breast cancer histology images with deep neural networks. In *MICCAI*.

Cooper, L., Sertel, O., Kong, J., et al. (2009). Feature-based registration of histopathology images with different stains: An application for computerized follicular lymphoma prognosis. *Computer methods and programs in biomedicine*, 96.

Courtiol, P., Tramel, E. W., Sanselme, M., et al. (2018). Classification and disease localization in histopathology using only global labels: A weakly-supervised approach. *coRR*, abs/1802.02212.

Couture, H. D., Marron, J., Perou, C. M., et al. (2018). Multiple instance learning for heterogeneous images: Training a cnn for histopathology. *coRR*, abs/1806.05083.

Daisuke, K. and Shumpei, I. (2018). Machine learning methods for histopathological image analysis. *Computational and Structural Biotechnology Journal*, 16.

Deng, J., Dong, W., Socher, R., et al. (2009). Imagenet: A large-scale hierarchical image database. In *CVPR*.

Diba, A., Sharma, V., Pazandeh, A. M., et al. (2017). Weakly supervised cascaded convolutional networks. In *CVPR*.

Dice, L. R. (1945). Measures of the amount of ecologic association between species. *Ecology*, 26.

Dolz, J., Desrosiers, C., and Ben Ayed, I. (2018). 3D fully convolutional networks for subcortical segmentation in MRI: A large-scale study. *NeuroImage*.

Doshi-Velez, F. and Kim, B. (2017). Towards a rigorous science of interpretable machine learning. *coRR*, abs/1702.08608.

Doyle, S., Agner, S., Madabhushi, A., et al. (2008). Automated grading of breast cancer histopathology using spectral clustering with textural and architectural image features. In *Intern. Symposium on Biomedical Imaging: From Nano to Macro*.

Doyle, S., Hwang, M., Shah, K., et al. (2007). Automated grading of prostate cancer using architectural and textural image features. In *Intern. Symposium on Biomedical Imaging: From Nano to Macro*.

Doyle, S., Madabhushi, A., Feldman, M., et al. (2006a). A boosting cascade for automated detection of prostate cancer from digitized histology. In *MICCAI*.

Doyle, S., Rodriguez, C., Madabhushi, A., et al. (2006b). Detecting prostatic adenocarcinoma from digitized histology using a multi-scale hierarchical classification approach. In *Intern. Conf. of the IEEE Engineering in Medicine and Biology Society*.

Durand, T., Mordan, T., Thome, N., et al. (2017). Wildcat: Weakly supervised learning of deep convnets for image classification, pointwise localization and segmentation. In *CVPR*.

Durand, T., Thome, N., and Cord, M. (2015). MANTRA: Minimum Maximum Latent Structural SVM for Image Classification and Ranking. In *ICCV*.

Durand, T., Thome, N., and Cord, M. (2016). Weldon: Weakly supervised learning of deep convolutional neural networks. In *CVPR*.

Ehteshami Bejnordi, B., Veta, M., Johannes van Diest, P., et al. (2017). Diagnostic Assessment of Deep Learning Algorithms for Detection of Lymph Node Metastases in Women With Breast CancerMachine Learning Detection of Breast Cancer Lymph Node MetastasesMachine Learning Detection of Breast Cancer Lymph Node Metastases. *JAMA*, 318.

Everingham, M., Van Gool, L., Williams, C. K. I., et al. (2010). The pascal visual object classes (voc) challenge. *IJCV*, 88.

Feng, X., Yang, J., Laine, A. F., et al. (2017). Discriminative localization in cnns for weakly-supervised segmentation of pulmonary nodules. In *MICCAI*.

Frenay, B. and Verleysen, M. (2014). Classification in the presence of label noise: A survey. *TNNLS*, 25.

Gartner, L. P. and Hiatt, J. L. (2006). Color textbook of histology: with student consult online access.

Ge, W., Yang, S., and Yu, Y. (2018). Multi-evidence filtering and fusion for multi-label classification, object detection and semantic segmentation based on weakly supervised learning. In *CVPR*.

Gertych, A., Ing, N., Ma, Z., et al. (2015). Machine learning approaches to analyze histological images of tissues from radical prostatectomies. *Computerized Medical Imaging and Graphics*, 46.

Girshick, R. (2015). Fast r-cnn. In *ICCV*.

Gondal, W. M., Köhler, J. M., Grzeszick, R., et al. (2017). Weakly-supervised localization of diabetic retinopathy lesions in retinal fundus images. In *ICIP*.

Goodfellow, I., Bengio, Y., and Courville, A. (2016). *Deep Learning*. MIT Press. http://www.deeplearningbook.org.

Greenberg, S. D. (1984). *Computer-assisted image analysis cytology*. Karger, S Publishers.

Guillaud, M., Adler-Storthz, K., Malpica, A., et al. (2005). Subvisual chromatin changes in cervical epithelium measured by texture image analysis and correlated with hpv. *Gynecologic oncology*, 99.

Guillaud, M., Cox, D., Malpica, A., et al. (2004). Quantitative histopathological analysis of cervical intra-epithelial neoplasia sections: methodological issues. 26.

Gurcan, M., Pan, T., Shimada, H., et al. (2006). Image analysis for neuroblastoma classification: Hysteresis thresholding for cell segmentation.

Gurcan, M. N., Boucheron, L., Can, A., et al. (2009). Histopathological image analysis: A review. *IEEE reviews in biomedical engineering*, 2.

Hamilton, P., Anderson, N., Bartels, P., et al. (1994). Expert system support using bayesian belief networks in the diagnosis of fine needle aspiration biopsy specimens of the breast. *Journal of clinical pathology*, 47.

He, K., Zhang, X., Ren, S., et al. (2014). Spatial pyramid pooling in deep convolutional networks for visual recognition. In *ECCV*.

He, K., Zhang, X., Ren, S., et al. (2016). Deep residual learning for image recognition. In *CVPR*.

He, L. (2009). *Towards image understanding: deformable contour and graph-based image segmentation and recognition*. Lambert Academic Publishing.

He, L., Long, L. R., Antani, S., et al. (2010). Computer assisted diagnosis in histopathology. *Sequence and genome analysis: methods and applications*, 15.

He, L., Long, L. R., Antani, S., et al. (2012). Histology image analysis for carcinoma detection and grading. *Computer methods and programs in biomedicine*, 107.

Hipp, J. D., Fernandez, A., Compton, C. C., et al. (2011). Why a pathology image should not be considered as a radiology image. *Journal of pathology informatics*, 2.

Hou, L., Samaras, D., Kurc, T. M., et al. (2016). Patch-based convolutional neural network for whole slide tissue image classification. In *CVPR*.

Ilse, M., Tomczak, J. M., and Welling, M. (2018). Attention-based deep multiple instance learning. *coRR*, abs/1802.04712.

Izadyyazdanabadi, M., Belykh, E., Cavallo, C., et al. (2018). Weakly-supervised learning-based feature localization in confocal laser endomicroscopy glioma images. *coRR*, abs/1804.09428.

Janowczyk, A., Basavanhally, A., and Madabhushi, A. (2017). Stain normalization using sparse autoencoders (stanosa): Application to digital pathology. *Computerized Medical Imaging and Graphics*, 57.

Janowczyk, A. and Madabhushi, A. (2016). Deep learning for digital pathology image analysis: A comprehensive tutorial with selected use cases. *Jour. of pathology informatics*, 7.

Jia, Z., Huang, X., Eric, I., Chang, C., and Xu, Y. (2017). Constrained deep weak supervision for histopathology image segmentation. *IEEE transactions on medical imaging*, 36(11):2376–2388.

Jie, Z., Wei, Y., Jin, X., et al. (2017). Deep self-taught learning for weakly supervised object localization. In *CVPR*.

Jütting, U., Gais, P., Rodenacker, K., et al. (1999). Diagnosis and prognosis of neuroendocrine tumours of the lung by means of high resolution image analysis. *Analytical Cellular Pathology*, 18.

Kandemir, M. and Hamprecht, F. (2015). Computer-aided diagnosis from weak supervision: A benchmarking study. *Computerized medical imaging and graphics*, 42.

Kantorov, V., Oquab, M., Cho, M., et al. (2016). Contextlocnet: Context-aware deep network models for weakly supervised localization. In *ECCV*.

Kayser, G., Riede, U., Werner, M., et al. (2002). Towards an automated morphological classification of histological images of common lung carcinomas. *Elec J Pathol Histol*, 8.

Kieffer, B., Babaie, M., Kalra, S., et al. (2017). Convolutional neural networks for histopathology image classification: Training vs. using pre-trained networks. In *Intern. Conf. on Image Processing Theory, Tools and Applications*.

Kiernan, J. A. (1990). *Histological and histochemical methods: theory and practice*, volume 20. Pergamon press Oxford.

Kong, J., Sertel, O., Lozanski, G., et al. (2007a). Automated detection of follicular centers for follicular lymphoma grading. In *Advancing Practice, Instruction, and Innovation Through Informatics Conf.*

Kong, J., Shimada, H., Boyer, K., et al. (2007b). Image analysis for automated assessment of grade of neuroblastic differentiation. In *Intern. Symposium on Biomedical Imaging: From Nano to Macro*.

Krizhevsky, A., Sutskever, I., and Hinton, G. E. (2012). Imagenet classification with deep convolutional neural networks. In *NIPS*.

Lamprecht, M. R., Sabatini, D. M., and Carpenter, A. E. (2007). Cellprofiler™: free, versatile software for automated biological image analysis. *Biotechniques*, 42.

Li, Y. and Ping, W. (2018). Cancer metastasis detection with neural conditional random field. In *Medical Imaging with Deep Learning*.

Lin, M., Chen, Q., and Yan, S. (2013). Network in network. *coRR*, abs/1312.4400.

Lin, T.-Y., Maire, M., Belongie, S., et al. (2014). Microsoft coco: Common objects in context. In *ECCV*.

Lipton, Z. C. (2018). The mythos of model interpretability. *Queue*, 16.

Litjens, G., Kooi, T., Bejnordi, B. E., et al. (2017). A survey on deep learning in medical image analysis. *MIA*.

Liu, W., Anguelov, D., Erhan, D., et al. (2016). Ssd: Single shot multibox detector. In *ECCV*.

Madabhushi, A. (2009). Digital pathology image analysis: opportunities and challenges. *Imaging in medicine*, 1.

Marcus, G. (2001). *The algebraic mind: Integrating connectionism and cognitive science*. MIT Press.

Marcus, G. (2018). Deep learning: A critical appraisal. *CoRR*, abs/1801.00631.

Mescher, A. L. (2013). *Junqueira's basic histology: text and atlas*, volume 12. McGraw-Hill Medical.

Molnar, C. et al. (2018). Interpretable machine learning: A guide for making black box models explainable.

Mungle, T., Tewary, S., Das, D., et al. (2017). Mrf-ann: a machine learning approach for automated er scoring of breast cancer immunohistochemical images. *Journal of microscopy*, 267.

Murphy, D. B. and Davidson, M. W. (2001). *Fundamentals of light microscopy and electronic imaging*, volume 184. Wiley Online Library.

Naik, S., Doyle, S., Madabhushi, A., et al. (2007). Automated gland segmentation and gleason grading of prostate histology by integrating low-, high-level and domain specific information. In *Workshop on Microscopic Image Analysis with Applications in Biology*.

Nelson, D. L., Lehninger, A. L., and Cox, M. M. (2008). *Lehninger principles of biochemistry*. Macmillan.

O'Neil, C. (2016). *Weapons of Math Destruction: How Big Data Increases Inequality and Threatens Democracy*. Crown Publishing Group.

Oquab, M., Bottou, L., Laptev, I., et al. (2015). Is object localization for free?-weakly-supervised learning with convolutional neural networks. In *CVPR*.

Otsu, N. (1979). A threshold selection method from gray-level histograms. *IEEE Trans. on Systems, Man, and Cybernetics*, 9.

Petushi, S., Garcia, F. U., Haber, M. M., et al. (2006). Large-scale computations on histology images reveal grade-differentiating parameters for breast cancer. *BMC medical imaging*, 6.

Pinheiro, P. H. O. and Collobert, R. (2015a). From image-level to pixel-level labeling with convolutional networks. In *CVPR*.

Pinheiro, P. O. and Collobert, R. (2015b). From image-level to pixel-level labeling with convolutional networks. In *CVPR*.

Quellec, G., Cazuguel, G., Cochener, B., and Lamard, M. (2017). Multiple-instance learning for medical image and video analysis. *IEEE reviews in biomedical engineering*, 10.

Qureshi, H., Sertel, O., Rajpoot, N., et al. (2008). Adaptive discriminant wavelet packet transform and local binary patterns for meningioma subtype classification. In *MICCAI*.

Redmon, J., Divvala, S. K., Girshick, R. B., et al. (2016). You only look once: Unified, real-time object detection. In *CVPR*.

Ribeiro, M. T., Singh, S., and Guestrin, C. (2016). "why should i trust you?": Explaining the predictions of any classifier. In *ACM SIGKDD 2016*.

Ronneberger, O., Fischer, P., and Brox, T. (2015). U-net: Convolutional networks for biomedical image segmentation. In *MICCAI*.

Ross, M., Kaye, G., and Pawlina, W. (2003). Histology a text and atlas.

Roux, L., Racoceanu, D., Loménie, N., et al. (2013). Mitosis detection in breast cancer histological images an icpr 2012 contest. *Jour. of pathology informatics*, 4.

Samek, W., Wiegand, T., and Müller, K.-R. (2017). Explainable artificial intelligence: Understanding, visualizing and interpreting deep learning models. *coRR*, abs/1708.08296.

Schroeder, W., Ng, L., and Cates, J. (2003). The itk software guide.

Sedai, S., Mahapatra, D., Ge, Z., et al. (2018). Deep multiscale convolutional feature learning for weakly supervised localization of chest pathologies in x-ray images. In *Intern. Workshop on Machine Learning in Medical Imaging*.

Selvaraju, R. R., Cogswell, M., Das, A., et al. (2017). Grad-cam: Visual explanations from deep networks via gradient-based localization. In *ICCV*.

Settles, B. (2009). Active learning literature survey. Technical report, University of Wisconsin-Madison Department of Computer Sciences.

Shah, M., Wang, D., Rubadue, C., et al. (2017). Deep learning assessment of tumor proliferation in breast cancer histological images. In *Intern. Conf. on Bioinformatics and Biomedicine*.

Sheikhzadeh, F., Guillaud, M., and Ward, R. K. (2016). Automatic labeling of molecular biomarkers of whole slide immunohistochemistry images using fully convolutional networks. *coRR*, abs/1612.09420.

Shen, Y., Ji, R., Zhang, S., et al. (2018). Generative adversarial learning towards fast weakly supervised detection. In *CVPR*.

Shimodaira, H. (2000). Improving predictive inference under covariate shift by weighting the log-likelihood function. *Journal of statistical planning and inference*, 90.

Sirinukunwattana, K., Pluim, J. P., Chen, H., et al. (2017). Gland segmentation in colon histology images: The glas challenge contest. *MIA*, 35.

Spanhol, F. A., Oliveira, L. S., Petitjean, C., et al. (2016a). Breast cancer histopathological image classification using convolutional neural networks. In *IJCNN*.

Spanhol, F. A., Oliveira, L. S., Petitjean, C., et al. (2016b). A dataset for breast cancer histopathological image classification. *IEEE Trans. on Biomedical Engineering*, 63.

Sternberg, S. (1997). *Histology for pathologists*, volume 757. Lippincott-Raven Philadelphia.

Su, W., Yuan, Y., and Zhu, M. (2015). A relationship between the average precision and the area under the roc curve. In *Int. Conf. on The Theory of Information Retrieval*.

Sudharshan, P., Petitjean, C., Spanhol, F., et al. (2019). Multiple instance learning for histopathological breast cancer image classification. *Expert Systems with Applications*, 117.

Sugiyama, M. and Kawanabe, M. (2012). *Machine learning in non-stationary environments: Introduction to covariate shift adaptation*. MIT press.

Sukhbaatar, S., Bruna, J., Paluri, M., et al. (2014). Training convolutional networks with noisy labels. *coRR*, abs/1406.2080.

Sun, C., Paluri, M., Collobert, R., et al. (2016). Pronet: Learning to propose object-specific boxes for cascaded neural networks. In *CVPR*.

Sun, K., Zhao, Y., Jiang, B., Cheng, T., Xiao, B., Liu, D., Mu, Y., Wang, X., Liu, W., and Wang, J. (2019). High-resolution representations for labeling pixels and regions. *CoRR*, abs/1904.04514.

Szegedy, C., Vanhoucke, V., Ioffe, S., et al. (2016). Rethinking the inception architecture for computer vision. In *CVPR*.

Szegedy, C., Zaremba, W., Sutskever, I., et al. (2013). Intriguing properties of neural networks. *coRR*, abs/1312.6199.

Tabesh, A., Teverovskiy, M., Pang, H.-Y., et al. (2007). Multifeature prostate cancer diagnosis and gleason grading of histological images. *IEEE trans. on medical imaging*, 26.

Tang, J., Rangayyan, R. M., Xu, J., et al. (2009). Computer-aided detection and diagnosis of breast cancer with mammography: recent advances. *IEEE Trans. on Information Technology in Biomedicine*, 13.

Tang, P., Wang, X., Bai, X., et al. (2017). Multiple instance detection network with online instance classifier refinement. In *CVPR*.

Tang, P., Wang, X., Wang, A., et al. (2018). Weakly supervised region proposal network and object detection. In *ECCV*.

Teh, E. W., Rochan, M., and Wang, Y. (2016). Attention networks for weakly supervised object localization. In *BMVC*.

Török, P. and Kao, F. (2007). *Optical imaging and microscopy: techniques and advanced systems*, volume 87. Springer.

Uijlings, J. R., Van De Sande, K. E., Gevers, T., et al. (2013). Selective search for object recognition. *IJCV*, 104.

Van de Sande, K. E., Uijlings, J. R., Gevers, T., et al. (2011). Segmentation as selective search for object recognition. In *ICCV*.

Veta, M., Heng, Y. J., Stathonikos, N., et al. (2018). Predicting breast tumor proliferation from whole-slide images: the tupac16 challenge. *coRR*, abs/1807.08284.

Veta, M., Pluim, J., Van Diest, P. J., et al. (2014). Breast cancer histopathology image analysis: A review. *IEEE Transactions on Biomedical Engineering*, 61.

Wan, F., Wei, P., Jiao, J., et al. (2018). Min-entropy latent model for weakly supervised object detection. In *CVPR*.

Wang, C., Ren, W., Huang, K., et al. (2014). Weakly supervised object localization with latent category learning. In *ECCV*.

Wang, D., Foran, D. J., Ren, J., et al. (2015). Exploring automatic prostate histopathology image gleason grading via local structure modeling. In *Intern. Conf. the IEEE Engineering in Medicine and Biology Society*.

Wang, X., Yan, Y., Tang, P., Bai, X., and Liu, W. (2018). Revisiting multiple instance neural networks. *Pattern Recognition*, 74.

Weind, K. L., Maier, C. F., Rutt, B. K., et al. (1998). Invasive carcinomas and fibroadenomas of the breast: comparison of microvessel distributions–implications for imaging modalities. *Radiology*, 208.

Wootton, R., Springall, D., Polak, J. M., et al. (1995). *Image analysis in histology*. CUP Archive.

Xie, J., Liu, R., Joseph Luttrell, I., et al. (2019). Deep learning based analysis of histopathological images of breast cancer. *Frontiers in genetics*.

Xu, J., Luo, X., Wang, G., et al. (2016). A deep convolutional neural network for segmenting and classifying epithelial and stromal regions in histopathological images. *Neurocomputing*, 191.

Yoo, T. S. (2004). *Insight into images: principles and practice for segmentation, registration, and image analysis*. AK Peters/CRC Press.

Zhang, C., Bengio, S., Hardt, M., et al. (2017). Understanding deep learning requires rethinking generalization. *CoRR*, abs/1611.03530.

Zhang, J., Bargal, S. A., Lin, Z., et al. (2018a). Top-down neural attention by excitation backprop. *IJCV*, 126.

Zhang, Q.-C. and Zhu, S.-C. (2018). Visual interpretability for deep learning: a survey. *Frontiers of Information Technology & Electronic Engineering*, 19:27–39.

Zhang, X., Wei, Y., Feng, J., et al. (2018b). Adversarial complementary learning for weakly supervised object localization. In *CVPR*.

Zhou, B., Khosla, A., Lapedriza, A., et al. (2016). Learning deep features for discriminative localization. In *CVPR*.

Zhou, Z.-H. (2004). Multi-instance learning: A survey. *Department of Computer Science & Technology, Nanjing University, Tech. Rep*.

Zhou, Z.-H. (2017). A brief introduction to weakly supervised learning. *NSR*.

Zhu, Y., Zhou, Y., Ye, Q., et al. (2017). Soft proposal networks for weakly supervised object localization. In *ICCV*.

Zitnick, C. L. and Dollár, P. (2014). Edge boxes: Locating object proposals from edges. In *ECCV*.

A Visual results of pixel-wise localization of regions of interest

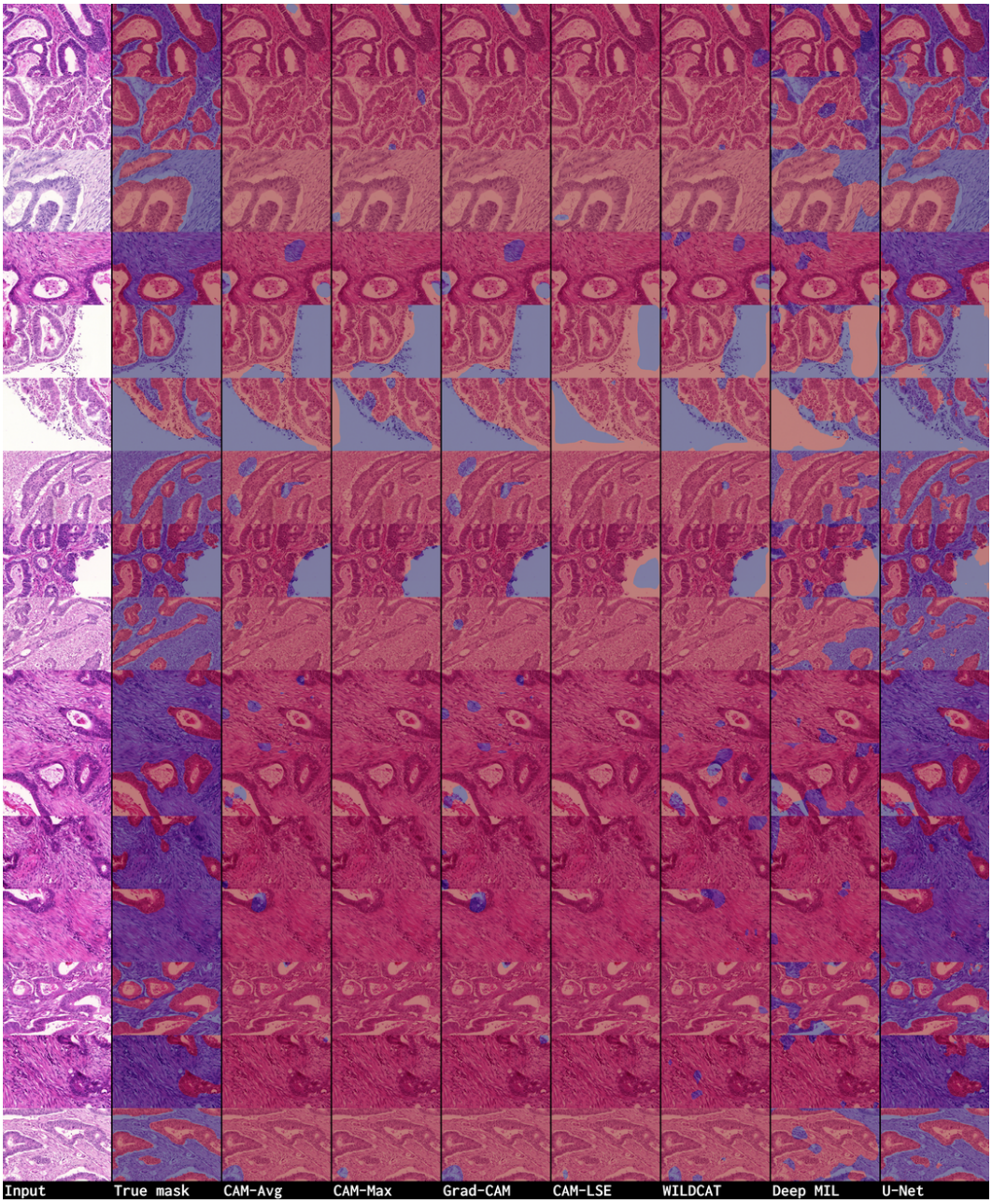

Figure 17: Examples of visual comparison of the predicted binary mask of each deep WSL method over GlaS test set (first split) for the malignant class. (Best visualized in color.)

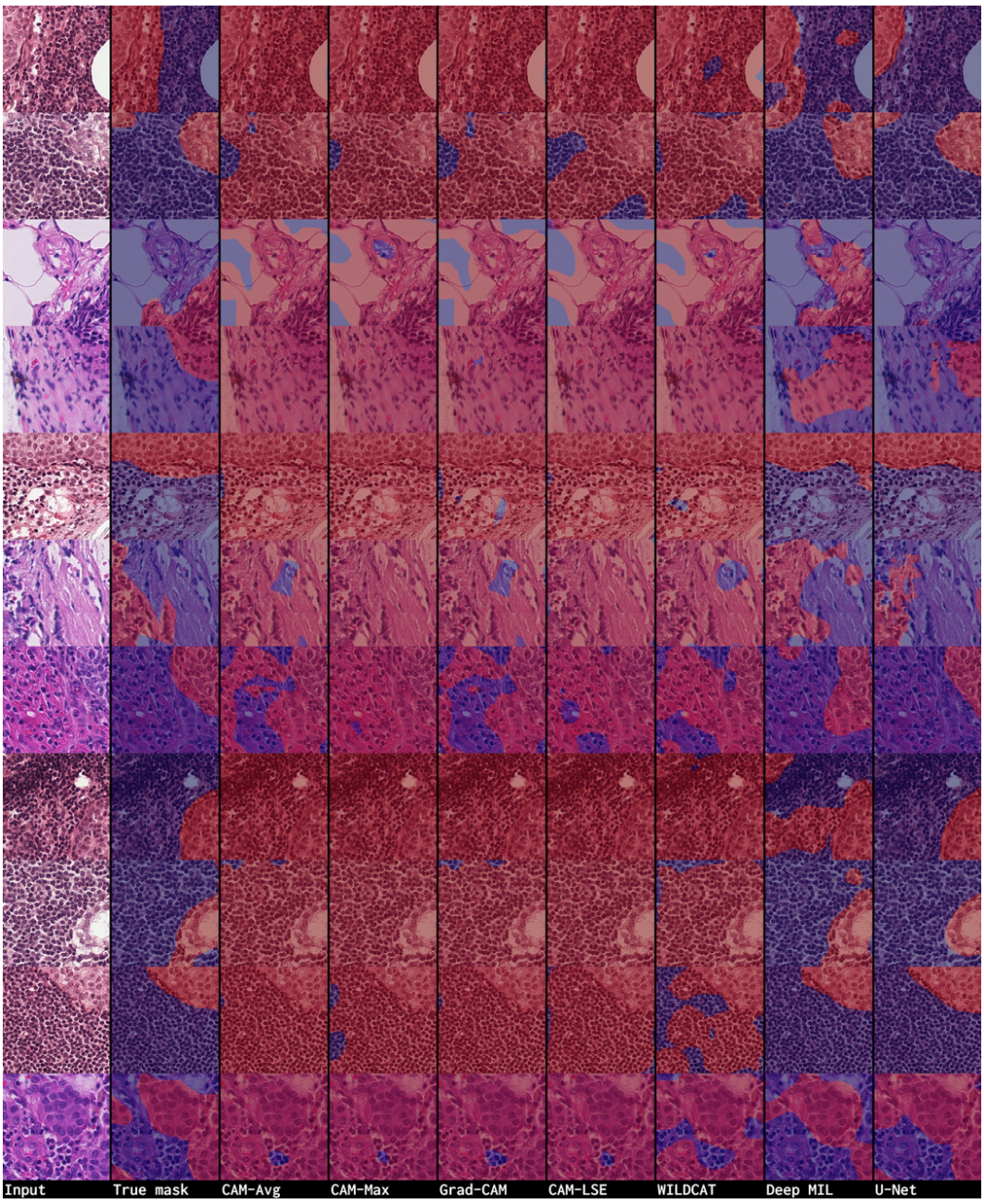

Figure 18: Examples of visual comparison of the predicted binary mask of each deep WSL method over CAMELYON16 test set (first split) for the metastatic class (patch size 512×512). (Best visualized in color.)

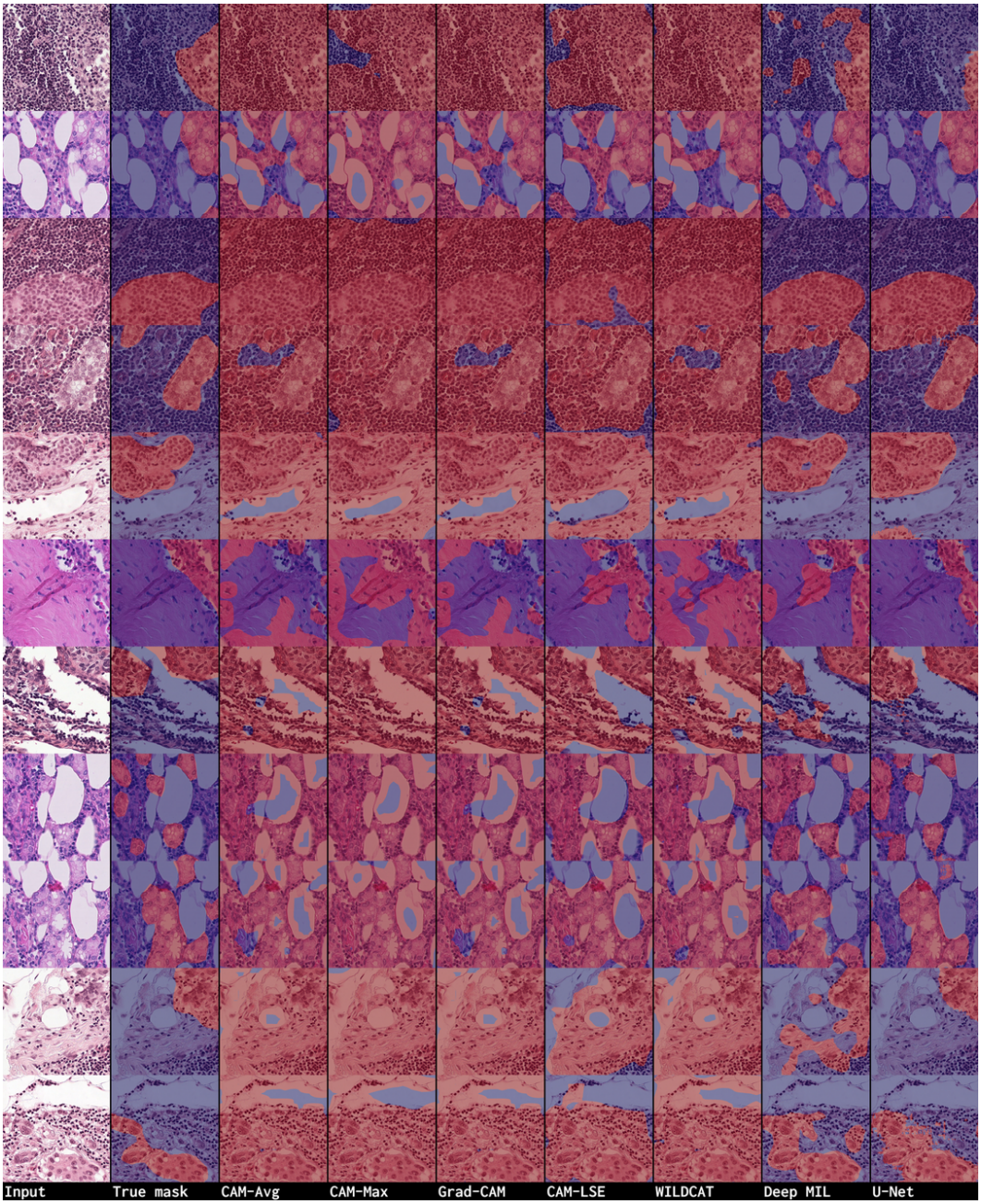

Figure 19: Examples of visual comparison of the predicted binary mask of each deep WSL method over CAMELYON16 test set (first split) for the metastatic class (patch size 768×768). (Best visualized in color.)

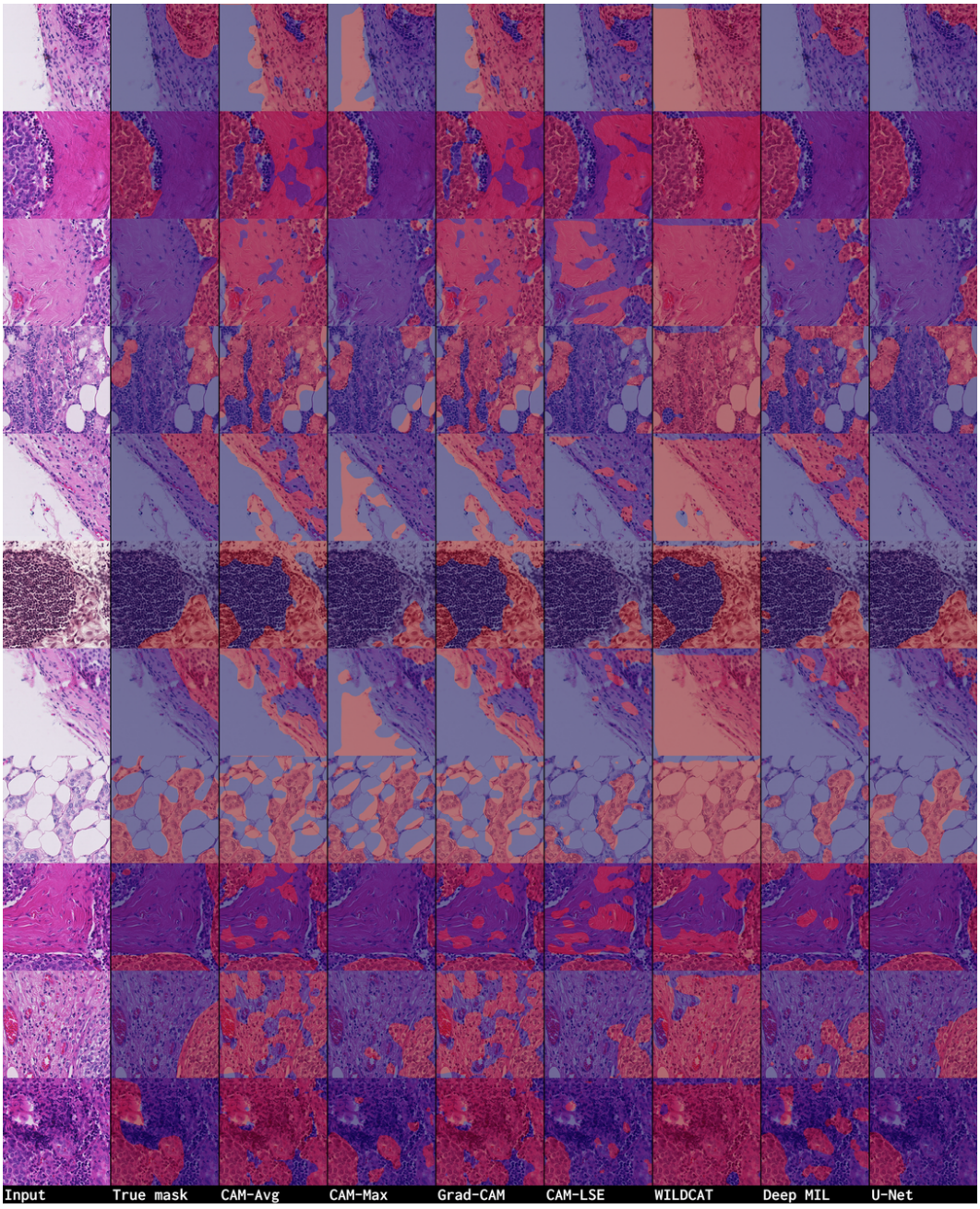

Figure 20: Examples of visual comparison of the predicted binary mask of each deep WSL method over CAMELYON16 test set (first split) for the metastatic class (patch size $1\,024 \times 1\,024$). (Best visualized in color.)